University of Zurich[UZH]

Towards detection and understanding of paraglacial landslides in Southern Alaska using surface velocity data and deep learning

GEO 511 Master's Thesis

Author
Jérôme Messmer
19-108-554

Supervised by
Jane Walden (walden@vaw.baug.ethz.ch)
Prof. Dr. Livia Piermattei

Faculty representative
Prof. Dr. Andreas Vieli

01.02.2025
Department of Geography, University of Zurich

GEO 511 Master's Thesis

Towards detection and understanding of paraglacial landslides in Southern Alaska using surface velocity data and deep learning

Jérôme Messmer
19-108-554

31.01.2025

Supervised by
Jane Walden (walden@vaw.baug.ethz.ch)
Prof. Dr. Livia Piermattei

Faculty representative
Prof. Dr. Andreas Vieli

Department of Geography, University of Zurich

Universität Zürich[UZH]

Glacier mass loss results in destabilization of adjacent slopes. In Southern Alaska in particular, the combination of amplified glacier mass loss and fjord environments pose a potential cascading tsunami hazard that may intensify. This study utilizes the ITS_LIVE glacier velocity dataset, which covers glacier-adjacent areas, to detect landslides. The research involves manual mapping and investigates the potential of deep learning techniques for landslide detection using this dataset, while also analyzing the environmental factors that influence landslide occurrence. A total of 182 paraglacial landslides were identified, confirmed, and manually mapped across Southern Alaska. However, the detection likely only captures landslides with pronounced activity, and data quality issues may are present. Despite these limitations, the dataset proves valuable due to its accessibility and broad coverage. An initial deep learning-based landslide detection algorithm shows promising results in some areas but performs less effectively in others (Precision: 0.25, Recall: 0.53, F1 Score: 0.29, Mean IoU: 0.34). Key challenges include noise, a limited training dataset, and the need for careful selection of input data channels. Analysis of the mapped landslides reveals a preferential occurrence in areas where glaciers are experiencing above-average mass loss, suggesting a potential link between glacial dynamics and landslide activity. Additionally, landslides are more common in regions with higher annual precipitation, indicating a possible connection between wet climate and slope destabilization. Permafrost does not appear to be a major factor at most sites, while the lithology aligns with known susceptibilities.

Contents

List of Figures

List of Tables

List of Abbreviations

CNN Convolutional Neural Network

DInSAR Differential Interferometric Synthetic Aperture Radar

DEM Digital Elevation Model

FPN Feature Pyramid Network

InSAR Interferometric Synthetic Aperture Radar

ITS_LIVE Inter-Mission Time Series of Land Ice Velocity and Elevation project

LIA Little Ice Age

LiDAR Light Detection and Ranging

MAGT Mean Annual Ground Temperature

MAGT Multitemporal Interferometric Synthetic Aperture Radar

NIR Near-Infrared

PRISM Parameter-elevation Relationships on Independent Slopes Model

RGB Red, Green, Blue

RGI Randolph Glacier Inventory

R-CNN Region-based Convolutional Neural Network

ROI Region Of Interest

RPN Region Proposal Network

SAR Synthetic Aperture Radar

UAV Unoccupied Aerial Vehicle

Acknowledgements

I would like to express my gratitude to the people who contributed to this project.

I would like to thank Jane Walden for her cordial and engaged guidance, recommendations, and valuable input throughout the project, and the opportunity to work on this interesting topic.

Prof. Dr. Livia Piermattei provided essential supervision, insightful feedback, and continuous support, which I am grateful for.

Prof. Dr. Andreas Vieli is thanked for serving the role as a faculty member, and the valuable insights shared during the concept presentation were greatly appreciated.

Dr. Bretwood Higman, Dr. Romain Hugonnet, Dr. Alex Gardner, and Alessandro De Pedrini are thanked for their informative correspondence related to this project.

I thank Planet Labs for granting me project access to Planet imagery, valuable in this project.

I am also grateful to Lukas Kugler for his spontaneous, helpful insights during a progress meeting.

I thank the VAW glaciology group at the Swiss Federal Institute of Technology for their warm environment, engaging discussions, and weekly Zopf, I enjoyed during this project.

Finally, I thank my friends and family for their relentless support and inspiration.

1. Introduction

Glaciers in high mountain regions are rapidly losing mass due to anthropogenic climate change (Hugonnet et al., 2021; Marzeion et al., 2014). As they recede, they expose landscapes that have not yet adjusted to non-glacial conditions (Ballantyne, 2002; Church & Ryder, 1972). An important process in this geomorphic adjustment is landsliding, which has been linked to glacier mass loss in numerous studies (e.g., Allen et al., 2011; Caine, 1982; Cossart et al., 2008; Holm et al., 2004). While much research has focused on the debuttressing process — where the removal of lateral support by glacier ice is assumed to trigger slope failures — this concept has been challenged. Glacier ice deforms under low stresses, which may limit landslide movement rather than prevent it (McColl et al., 2010; McColl & Davies, 2013). More recent research has explored connections between glacier change, and landslide kinematics in specific locations, such as Barry Arm, Alaska (Dai et al., 2020; Schaefer et al., 2023), and Moosfluh in the Swiss Alps (e.g. Glueer et al., 2020; Grämiger et al., 2017; Storni et al., 2020). However, fewer have offered a more regional perspective.

Southern Alaska offers a particularly relevant case for studying paraglacial landslides, given its steep topography, seismic activity (Brueseke et al., 2019), and glacier mass loss which is amplified in global comparison (Hugonnet et al., 2021). The region's fjords, where landslides can generate tsunamis, pose substantial hazards. Notable past events include a landslide in Lituya Bay in 1958 that triggered a tsunami with a run-up height exceeding 500 meters, resulting in two fatalities (Miller, 1960). Additional major landslide-triggered tsunamis have been recorded near Grewingk Glacier in Kachemak Bay in 1967 (Lemaire et al., 2024; Wiles & Calkin, 1992), and Taan Fjord in 2015 (Haeussler et al., 2018; Higman et al., 2018), and potential for furher landslide triggered tsunami has been found by Schaefer et al. (2024) for the Prince William Sound region. With continuing glacier mass loss (Wahr et al., 2016), concerns arise if paraglacial landslides could increase in frequency and with that bring an increased tsunami hazard potential.

The need for better knowledge of the distribution of paraglacial landslides is important, both to advance knowledge about landslide response to glacier mass loss and to support hazard mitigation efforts. The Inter-Mission Time Series of Land Ice Velocity and Elevation project (ITS_LIVE) surface velocity dataset (Gardner, Fahnstock, & Scambos, 2024; Gardner et al., 2018) generated through feature tracking of satellite imagery presents a promising opportunity to address this need. Originally developed for quantification of glacier surface velocities, it also captures surface velocities of the surrounding terrain, making it a potentially valuable source for identifying landslides. The coverage of glaciated regions around the world eliminates the need for additional processing. The presence of active landslides in the data has been demonstrated by Walden et al. (2024), who monitored the evolution of several landslides in Southcentral Alaska in response to glacier change, but its value for landslide detection remains largely unused and unexamined.

This study seeks to build on the capabilities of the ITS_LIVE dataset by using it to create a regional inventory of paraglacial landslides in Southern Alaska. Based on the challenges encountered and comparison to inventories derived from other sources, an assessment of its limitations is made.

Motivated by the large-scale global availability of the data, the study examines the feasibility of automated landslide detection based on ITS_LIVE using a Convolutional Neural Network (CNN) trained on the manually mapped detections. CNNs have shown promise in landslide detection tasks in other contexts (Ghorbanzadeh et al., 2019; Oak et al., 2024). The study especially aims to explore different input data variations, to make recommendations for future development.

Building on the manual detections, this study will also investigate how environmental factors influence landslide occurrence. Beyond glaciation, factors such as lithology (e.g., Brideau et al., 2009; Fischer et al., 2006), permafrost dynamics (Deline et al., 2021; Matsuoka & Murton, 2008), and the impact of precipitation on weathering and rock mechanics (Iverson, 2000; Le Roux et al., 2009) are important factors in paraglacial slope stability. This investigation will provide an overview of these factors across the detected landslides, with a focus on identifying broad patterns, rather than offering detailed, site-specific analyses.

Following, this study aims to answer the following research questions:

- How effective can active paraglacial landslides be detected manually using ITS_LIVE surface velocity data, and what are the associated limitations?
- How effective is a convolutional neural network trained on the manually mapped paraglacial landslides, ITS_LIVE surface velocity data and auxiliary data in a landslide detection task, and how can its performance be improved?
- What are the connections between the occurrence of the manually detected paraglacial landslides and spatial patterns in glacier mass loss, precipitation, permafrost distribution, and lithology?

To answer these questions, this study will perform manual mapping, offer a description of the limitations faced in this process and compare the detected landslides to available inventories. It further implements a convolutional neural network, conducting sensitivity tests to different input data cases and assesses the patterns in occurrence of the landslides using large scale environmental datasets.

2. Theoretical background

2.1. Paraglacial geomorphology

The concept of paraglacial geomorphology was introduced by Church and Ryder (1972, p. 3059) to describe "nonglacial processes that are directly conditioned by glaciation." Associated with this concept is the paraglacial period, which is the time period during which these processes are conditioned by prior glaciation. This concept highlights the instability or metastability of newly deglaciated landscapes. Following deglaciation, these landscapes undergo high rates of geomorphic change until adjustment to non-glacial conditions (Ballantyne, 2002; Church & Ryder, 1972). Processes active in this adjustment period encompass slope movements, aeolian, fluvial, lacustrine, coastal and marine processes (Ballantyne, 2002; Slaymaker, 2009, 2011).

A major criticism of the concept of paraglacial geomorphology is the ambiguity stemming from the broad range and indefinite nature of the timescales associated with paraglacial landscape adjustment (Eyles & Kocsis, 1989). Further confusion arises from the widespread overlap in the usage of the terms paraglacial, proglacial, and periglacial. Proglacial describes geomorphological processes and landforms spatially, relating their proximity to glacier margins (Slaymaker, 2009). Periglacial refers to non-glacial processes in a cold climate and their resulting landforms (French, 2007). However, there is overlap as paraglacial geomorphology includes proglacial areas and may involve periglacial processes.

Despite the ambiguity in the relevant temporal scales involved and the overlap with related concepts, paraglacial geomorphology — understood as the rate and trajectory of geomorphic change following deglaciation — remains valuable for understanding geomorphic changes driven by past glaciation (Slaymaker, 2009, 2011).

2.2. Slope movements

Slope movements are defined as the movement of rock, earth or debris down a slope (Cruden, 1991). Slope movements are also referred to as landslides even in the absence of sliding mechanisms. The terms slope movement, landslide and slope instability are used interchangeably in literature and in this work.

Slope movements are dynamic systems which develop over time. The development of most slope movements can be described in stages, as outlined by Leroueil and Locat (1998): (1) pre-failure deformation, characterized by initial and gradual deformations; (2) failure, characterized as the most significant phase in terms of displacement and movement rate; and (3) post-failure behavior, influenced primarily by structural and morphological changes resulting from failure. If no movement occurs within a defined period – usually one year – a slope movement is considered inactive. When a previously inactive slope movement resumes activity, it is classified as reactivated (Cruden & Varnes, 1996), with reactivation representing a possible fourth stage in the framework of Leroueil and Locat (1998). However, activity patterns and developmental stages may vary across different segments of the same slope movement. In this study, a slope movement is considered active when movement rates are high enough to be detected with the employed methods.

Several approaches have been taken to develop a standardized terminology for the diverse processes classified as slope movement. The prominent classification scheme of Varnes (1978), critically revised by Hungr et al. (2014), classifies slope movements by the type of movement and the geotechnical characteristics of the displaced material. In particular, Hungr et al. (2014) subdivide the movement types into falling, toppling, sliding (which is further subdivided by the geometry of the sliding surface), spreading, flowing and slope deformation. Additionally, materials are categorized as bedrock or unconsolidated material (rock/soil in Hungr et al. (2014)). Unconsolidated material is further distinguished following geotechnical classifications. While these classifications offer useful terminology, it is important to recognize that slope movements can involve combinations of movement types and materials, which may evolve throughout different development stages.

2.3. Paraglacial slope stability

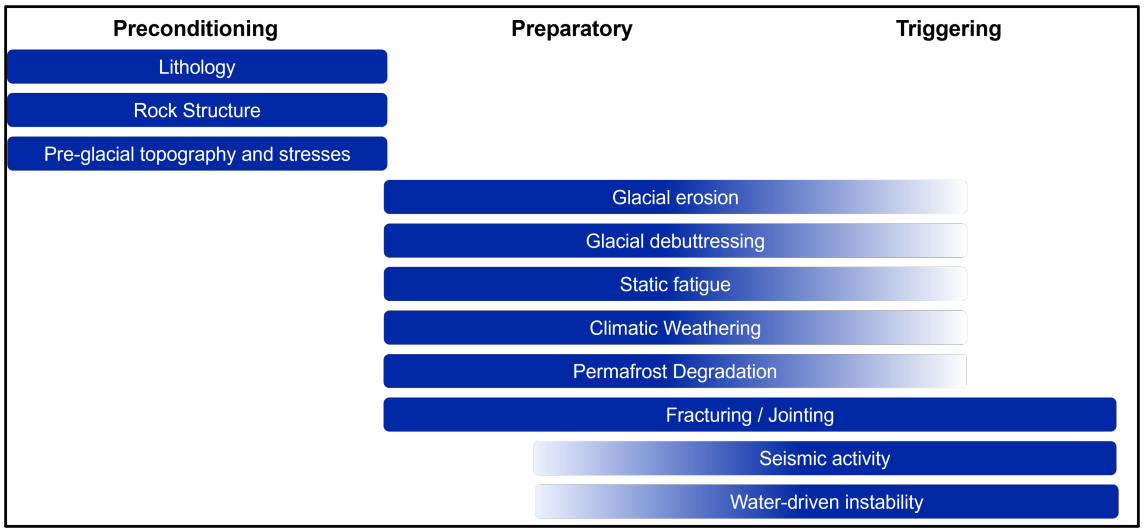

Figure 1: Factors influencing paraglacial slope stability, as adapted from McColl (2012). Gradations represent their relative importance and certainty in their relevance based on qualitative assessments originally made by McColl (2012), with further adjustments applied in this adaptation.

Slope movements have been identified with increased frequency in areas affected by glacier retreat (e.g. Allen et al., 2011; Caine, 1982; Cossart et al., 2008; Holm et al., 2004). Many studies have focussed on linking slope movements to glacier retreat temporally, finding such links across Holocene (e.g. Bell, 1976; Ivy-Ochs et al., 2009; Le Roux et al., 2009) as well as historic (e.g. Bovis, 1982; Holm et al., 2004) timescales. Further work has also indicated influence of glacier recession on recent activation and failure of slope movement (e.g. Dai et al., 2020; Fischer et al., 2010; Huggel et al., 2012; Ravanel & Deline, 2011; Schaefer et al., 2023; Walden et al., 2024).

A conceptual model introduced by Glade and Crozier (2005) helps describe the factors influencing slope destabilization in response to glacier recession. This model distinguishes between preconditioning, preparatory, and triggering factors. Preconditioning factors are

static, inherent properties that influence the margin of stability and predispose the slope to further destabilizing. Preparatory factors are dynamic influences that shift a slope from a stable to a marginally stable state. Triggering factors overcome this margin of stability, initiating movement. The distinction between preparatory and triggering factors can be ambiguous, as various factors may both bring a slope close to the margin of stability and surpass it. An overview of the factors influencing paraglacial slope stability is given in Figure 1.

Preconditioning factors that contribute to slope instability include various litho-structural properties, such as the lithological composition of the bedrock, layering, and preexisting structural features like fractures, joints, or foliation (Augustinus, 1995; Bovis, 1982; Brideau et al., 2009; Fischer et al., 2006; Thorarinsson et al., 1959). Additionally, the topography existing prior to glaciation and the pre-existing stress regime are regarded as preconditioning factors (McColl, 2012).

Dynamic factors that contribute to the destabilization or occasionally trigger the failure of rock slopes in paraglacial land systems include glacial erosion, which can lead to steep relief and the exposure of rock weaknesses (Augustinus, 1995; Grämiger et al., 2017). In addition, glacier retreat and glacial erosion of overlying rock result in stress redistribution within rock slopes (Cossart et al., 2008; Grämiger et al., 2017), which in turn leads to the formation and expansion of fractures. These fractures, typically oriented in a slope-parallel or subparallel orientation, further promote instability (Fischer et al., 2010; Grämiger et al., 2017; Nichols, 1980). Moreover, static fatigue, which is the gradual weakening of rock masses under stress levels below their fracture strength, contributes to slope instability. This effect is particularly pronounced when combined with stress redistribution, as the mechanisms causing static fatigue are amplified non-linearly by increasing stress levels (Brideau et al., 2009; Molnar, 2004). Finally, seismic activity, which is intensified by isostatic rebound resulting from glacial erosion and deglaciation, may further weaken the rock mass, and potentially trigger landslides (Sanchez et al., 2010; Thorarinsson et al., 1959).

Climatic factors, which can also be linked to glacier change, include changing precipitation and meltwater regimes. These factors can enhance the erosivity of (glacio-)fluvial systems, undercutting river-adjacent slopes, and influence slope destabilization by changing infiltration rates and thus increasing pore water pressures, which may trigger landslides (Huggel et al., 2010; Huggel et al., 2012; Le Roux et al., 2009). Changes in climate further change rates of temperature-driven weathering including mechanical, chemical and biological weathering processes (Hall & Thorn, 2014; Matsuoka & Murton, 2008; Viles, 2013). Climatic factors also influence permafrost occurrence and through that slope destabilization that occurs in response warming and degradation of permafrost through several processes. These processes include weakening and loss of ice/rock interlocking, ice segregation, increased pore water pressures if meltwater remains undrained, increased deformation within ice fractions of the permafrost and frost wedging (Davies et al., 2001; Deline et al., 2021; Krautblatter et al., 2013; Matsuoka & Murton, 2008).

2.3.1. Debuttressing and landslide activation in response to glacier change

The process of debuttressing, which describes the removal of lateral support of adjacent slopes by glaciers, has been highlighted by Ballantyne (2002) as another critical factor in explaining the occurrence of paraglacial landslides following glacier retreat. However, the significance of this mechanism has been challenged by McColl et al. (2010), who argue that the ductile deformation of ice at low strain rates, coupled with basal water pressure, significantly reduces the effective resistivity of the ice, especially in temperate glaciers. McColl and Davies (2013) demonstrated – through mechanical analysis and field examples from New Zealand – that landslide protrusion into the glacier ice is possible due to elastic and plastic deformation of the ice mass. However, the resisting force of the ice limits the deformation velocity of slope instabilities relative to the applied stress, which is largely dependent on the landslide mass.

Recent studies have further explored the relationship between glacier mass loss and landslide activation, emphasizing the role of glacier thinning and retreat as important factors. For instance, Lacroix et al. (2022) found that the acceleration of landslide velocities in the Tungnakvíslarjökull area in Iceland was driven by a sudden increase in glacier thinning and retreat. Similarly, Dai et al. (2020) observed a strong correlation between landslide velocity and glacier retreat and thinning for a landslide in Barry Arm, Alaska. Schaefer et al. (2023) have observed differences in the kinematic behavior of the same landslide, depending on the position of the adjacent glacier, based on geomorphological interpretations. Extending these findings, Walden et al. (2024) assessed eight landslides in southern coastal Alaska, noting that glacier retreat beyond the landslide toe was a significant factor for half of the cases, while glacier thinning and high monthly precipitation were linked to the activation of two others.

A connection between landslide acceleration and glacier retreat has also been observed for the Moosfluh landslide in the Swiss Alps, where (Glueer et al., 2020) reported connections between glacier retreat and the kinematics and structural evolution of the landslide. For the same site Grämiger et al. (2017, 2018, 2020) used modelling to explore how glacial erosion and the cycles of glacier retreat and advance progressively destabilize rock slopes through mechanical, thermomechanical and hydromechanical stresses. Kos et al. (2016) further suggested that the activation of this critically stressed landslide is likely tied to the crossing of a threshold of ice loss, and Storni et al. (2020) linked its deformation velocity to glacier thinning.

2.4. Hazards connected to paraglacial landslides

The direct hazardous impact of landslides include destruction of infrastructure, loss of life, injury, and homelessness. However, these direct impacts are typically limited to the immediate vicinity of a landslide. Glaciated regions, such as Southern Alaska, are often sparsely populated have only limited infrastructure, reducing the immediate risks.

However, cascading processes triggered by landslides can extend the hazards posed by landslides far beyond their proximity. Landslide-dammed rivers and the subsequent breaching of these dams can result in catastrophic flooding events (Fan et al., 2020;

Gill & Malamud, 2014). Landslides also provide significant volumes of sediment, which, if mobilized, can generate debris flows downstream (Huggel et al., 2010; Iverson et al., 1997). A further cascading hazard posed by landslides is the generation of tsunamis, which are triggered when subaqueous or subaerial landslides fail rapidly within or into bodies of water (Gill & Malamud, 2014; Løvholt et al., 2015).

2.5. Remote sensing methods for landslide detection

Remote sensing methods play an important role in the detection, monitoring, and susceptibility mapping of landslides (Casagli et al., 2023; Novellino et al., 2024; Tofani et al., 2013; Zhao & Lu, 2018; Zhong et al., 2020). Detection involves identifying the location and distribution of landslides, while monitoring focuses on assessing the development of known landslides over time. In susceptibility mapping, remotely sensed information is used to predict the likelihood of future landslides.

Overall, remote sensing data for landslide detection can be acquired from spaceborne, aerial (e.g., Unoccupied Aerial Vehicles (UAVs), airplanes), or ground-based platforms. Satellite and aerial approaches are preferred for large-area detection due to their broad coverage, while ground-based platforms are often used for monitoring of smaller sites (Casagli et al., 2023; Tofani et al., 2013).

Landslides are characterized by the absence of distinct, unifying spectral and morphological characteristics (Zhong et al., 2020). The appearance of landslide surfaces varies considerably due to factors such as vegetation growth, erosion and geologic characteristics of the host bedrock, leading to a lack of consistent spectral signatures. Similarly, the geomorphological differences between various types of landslides result in the absence of distinct unifying morphological features that are observable for all landslides. These inherent challenges make it difficult to define general rules for landslide detection, leading to a continued popularity of manual mapping, mainly utilizing multispectral imagery as well as DEMs. While experienced interpreters can usually identify landslides well on the basis of these sources, this process is labor-intensive and subject to interpreter bias (Tofani et al., 2013; Zhong et al., 2020).

Despite these challenges, several automatic approaches have been successfully implemented utilizing passive multispectral and actively sensed imagery (Michel et al., 1999; Scaioni et al., 2014; Zhong et al., 2020). These include methods that focus on classifying imagery on a per-pixel basis, such as supervised classification, thresholding, and pixel-level change detection. However, these methods are limited by their neglect of spatial context beyond single pixels. Thus, object-based image analysis has gained popularity for landslide recognition, making use of pixel groupings to reduce noise and make use of spatial context (Keyport et al., 2018; Scaioni et al., 2014). Again, other methods have focussed on image correlation to track landslide movement (Stumpf et al., 2017).

Although landslides do not exhibit distinct, unifying spectral or morphological characteristics, they are universally characterized by changes in terrain over time. Therefore, remote sensing approaches that focus on terrain change are promising. One such approach is the use of Synthetic Aperture Radar (SAR), which measures the amplitude and phase of

microwave radiation actively emitted and scattered back by the target surface. Amplitude relates to the reflectance of the target, while phase values are related to the distance between the sensor and the target (Casagli et al., 2023; Scaioni et al., 2014). As the terrain changes between different acquisitions, this distance changes, causing phase shifts. Differential Interferometric SAR (DInSAR) exploits these phase variations, enabling the detection of small terrain changes over large areas (Gabriel et al., 1989). This method offers advantages such as large-area coverage, the ability to detect a broad range of deformation rates, and cloud penetration. To address challenges such as atmospheric effects and changes to the target surface not related to terrain movement, such as vegetation growth, Multitemporal InSAR (MTInSAR) uses a range of SAR images taken at different times. MTInSAR identifies stable points, such as rock outcrops or anthropogenic structures, which consistently reflect signals and are assumed to be stable themselves (Crosetto et al., 2016). This stability helps in consistently and accurately detecting even small terrain changes. However, there are limitations, including the need for considerable data processing, fixed acquisition times in the case of spaceborne SAR, and ambiguities caused by the dependence of the interferometric measurements on the acquisition geometry. This means that only terrain deformation along the line of sight is measured, which complicates the detection of landslides depending on their aspect. Other SAR-based techniques do not directly infer terrain changes from phase shifts, but instead focus on the loss of coherence between SAR images acquired at different times. This loss may indicate landslides, either due to changes in the scattering properties or the geometry of the target (Burrows et al., 2019, 2020). While these methods are less explicit in identifying terrain changes, they still focus on detecting change overall, which can also serve as indicators of landslide activity. However, these methods also require considerable data processing, which needs to be considered in their application.

Further methods for detecting terrain changes include differencing of DEMs generated from Light Detection and Ranging (LiDAR), stereophotgrammetry, or InSAR for different timesteps (Casagli et al., 2023; Scaioni et al., 2014; Tofani et al., 2013). These methods offer advantages like potentially high spatial and temporal resolution, vegetation penetration (with LiDAR), and, depending on the platform, extensive area coverage. However, they require considerable data processing, and detection accuracy depends on the quality of the source DEMs. Additionally, expert interpretation is often needed to accurately identify landslides in the difference products.

2.6. Machine learning, deep learning and convolutional neural networks

Machine learning describes techniques that enable systems to improve their performance on specific tasks through experience. (Mitchell, 1997). Deep learning is a subset of machine learning and uses multi-layered artificial neural networks to model patterns in the data they are trained on (LeCun et al., 2015). Classical machine learning, in contrast, refers to techniques that use feature engineering and statistical techniques, including methods like support vector machines and decision trees (Hastie et al., 2009).

Convolutional Neural Networks (CNNs) are a type of neural network developed to process structured grid data, such as images (LeCun et al., 2015; Zhao et al., 2024). They enable different tasks, including image classification, where an object class is assigned to an entire image; object detection, where objects are located within an image; classification, which is assigning detections to object classes; semantic segmentation, which is determining which pixels belong to objects of a class; and instance segmentation, which is determining which pixels belong to a specific instance of an object. These abilities have led to their adoption for a wide range of computer vision tasks which include autonomous driving, face recognition, medical diagnosis and remote sensing (Li et al., 2022; Oak et al., 2024).

CNNs are composed of several components, which are involved in learning representations of the gridded input data and in making the final predictions (He et al., 2017; Zeiler & Fergus, 2013; Zhao et al., 2024) (see Fig 2a). (1) Convolutional layers (see Fig 2b) apply different filters to the input grids using convolution operations. These filters detect image features such as edges, textures, and gradients. As the number of layers increases, they extract more complex and abstract features. The convolutional layers produce feature maps, which are representations of the extracted features from the input data. (2) Pooling layers (see Fig 2c) are used to reduce the spatial dimensions of the input data, which helps to improve the computational efficiency and improves the model's ability to detect features independent of their exact position within the grid. (3) Fully connected layers are layers, where each processing element (neuron) is connected to every processing element of the previous layer. They help reduce the dimensionality of the grid data, which is needed to generate the final object detection and classification results. Different types of non-linear activation functions determine which information is passed between the components of the model. This introduces non-linearity to the model, which improves the ability to represent complex features.

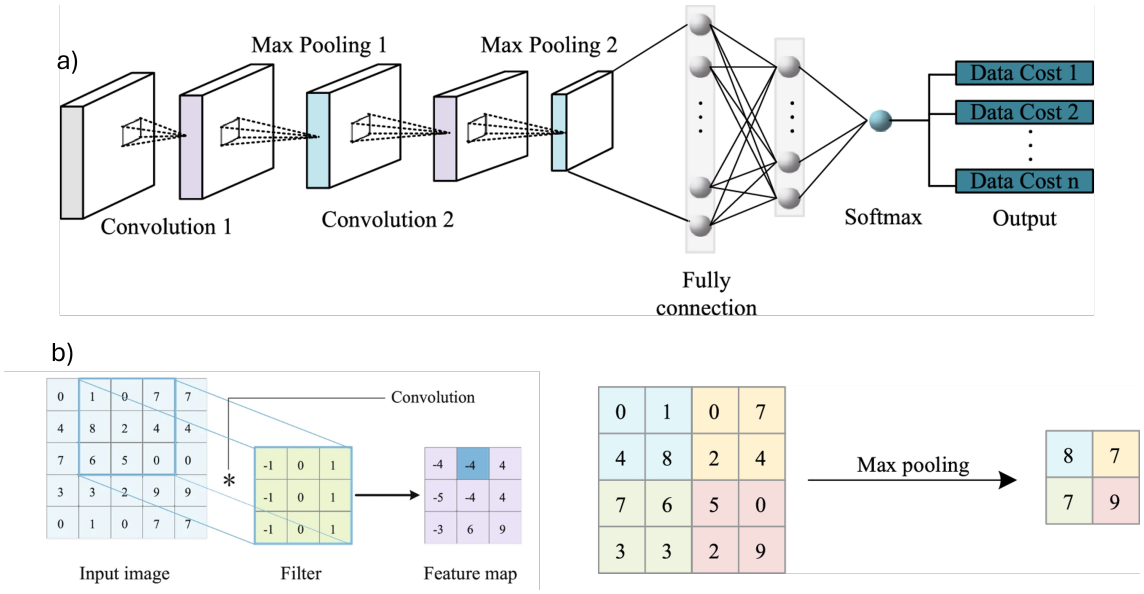

Figure 2: a) Schematic overview of a CNN with convolution and pooling operations, fully connected layers and a softmax function which computes a probability distributions of classes, b) schematic illustration of a convolution operation, and c) of a max pooling operation. Adapted after Zhao et al. (2024).

During training, the weights of the neural network are adjusted to minimize the difference between the model predictions and the ground truth. After each time data is passed through the model, a loss is calculated by comparing the model output with the ground truth. In backpropagation, the contribution of each weight to this loss is determined, which gives the gradients of the weights. These gradients are used to update the weights in the optimization step using gradient descent algorithms after each model run (Abdulla, 2017; He et al., 2017; Schmidhuber, 2015; Zhao et al., 2024). The adjusted weights include the weights of the different filters of the convolutional neural networks, as well as those of the connections of the fully connected layers. Additional weights vary by the specific models applied (Abdulla, 2017; He et al., 2017).

2.6.1. Use of machine learning and deep learning for landslide detection

Classical machine learning methods, including both pixel-based and object-based approaches, are widely used for landslide detection using remotely sensed data (Ghorbanzadeh et al., 2019; Tehrani et al., 2022; Zhong et al., 2020). These methods use either supervised or unsupervised classification techniques. In supervised classification, algorithms are trained on labeled data, such as pixels or pixel groupings, that have previously been classified. In unsupervised classification, pixels or pixel groupings are grouped into clusters based on their similarities. In the latter case, the resulting clusters require manual interpretation to identify the object classes.

However, classical machine learning methods face challenges in dealing with the lack of distinct, unifying spectral and morphological properties of landslides (Zhong et al., 2020). As a result, deep learning approaches, particularly CNNs, have become a popular choice for landslide detection due to their frequently superior performance compared to classical approaches, despite usually requiring more training data and computational resources (Ghorbanzadeh et al., 2019; Oak et al., 2024; Tehrani et al., 2022; Wang et al., 2021; Zhong et al., 2020). In general, CNNs are used to detect landslides, and create segmentation masks for landslides on the basis of various types of gridded input data and ground truth landslide bounding boxes or segmentation masks as an input.

There is great variation in the input data which has been used for the purpose of landslide detection using CNNs. Some studies focus only on true color imagery, often acquired using UAVs (e.g., Fu et al., 2022; Ullo et al., 2021). Some studies also incorporate multispectral data alongside auxiliary products. For example, Ghorbanzadeh et al. (2019) complement the use of the red, blue, green, and near-infrared (NIR) bands with the Normalized Difference Vegetation Index (NDVI), as well as slope, aspect, and terrain curvature maps. Shi et al. (2021) combine true color satellite imagery with road and building feature datasets to reduce misclassification between infrastructure and landslide features. Another approach that complements multispectral imagery with auxiliary data is the study of Liu et al. (2021) who additionally use a geologic map and DEM derivatives as training data.

The remotely sensed input data used in these studies goes beyond passive remote sensing products. Nava et al. (2021) used differently polarized SAR images, both pre- and post-event, in combination with DEMs, and slope maps as an input and compared it to a true-

color input. Liang et al. (2023) and Liu et al. (2022) utilized interferograms alongside multispectral satellite imagery and a DEM as training data, and Fang et al. (2022) relied on a DEM derived from airborne LiDAR and airborne true color imagery.

The choice of input data highlights that the distinction between detection and susceptibility mapping is often unclear in the data-driven nature of these models. For example, input data such as DEMs can both show geomorphological features of landslides but also provide information about landslide susceptibility through slope characteristics. Overall, however, these approaches demonstrate the effectiveness of CNNs for landslide detection, provided that well-selected input data that is informative about landslide occurrence and a matching ground-truth dataset of sufficient size is available.

3. Study area

This study focuses on the mountainous regions of Southeast and South-Central Alaska, including the Canadian portions of the coastal ranges and the Wrangell range. The Alaska Range and Aleutians were excluded to minimize time-intensive manual mapping. Subregions are distinguished based on the commonly accepted classification of mountain ranges (see Fig. 3).

The region is extensively glaciated. Glaciation includes vast ice fields and large valley glaciers. Mass loss rates of glaciers in Alaska exceed the global average and have notably accelerated in the 21st century (Hugonnet et al., 2021).

Southern and southeastern Alaska are largely made up of geologically diverse terranes which were accreted during the Mesozoic (see Fig. 3b). The active tectonic history has also led to the formation of terrane and forearc basins in which different marine sediments were deposited, and the formation of tectonic mélanges in accretionary wedges. The active tectonics have further driven the widespread formation of intrusive and extrusive rocks, the deposition of volcanic sediments, and have driven metamorphism of large rock units (Plafker & Berg, 1994; Wilson et al., 2015). Ongoing subduction continues to drive orogenic processes, locally active volcanism, and strong seismic activity (Brueseke et al., 2019). Quaternary glaciations left extensive surficial deposits, and influenced the steep mountainous and fjord topography through erosion. Little Ice Age (LIA) glacial advances started 700 BP, with the most pronounced advances in the mid 1700s and late 1800s (Calkin, 1988; Calkin et al., 2001).

The region's climate is highly variable. Coastal areas are characterized by oceanic and subpolar oceanic climates, while the interior mountainous regions are characterized by drier, colder subarctic and tundra climates (Daly et al., 2018) (see Fig. 3c). Climate warming has been particularly amplified in high latitudes and Alaska in particular (Bekryaev et al., 2010; Pithan & Mauritsen, 2014), resulting in warming of around twice the global average, largely attributable to anthropogenic influence (Walsh & Brettschneider, 2019). Precipitation has also increased in much of the study area in recent decades (White et al., 2021). and projections indicate continued increases in both mean annual temperature and precipitation (Mizukami et al., 2022) and an increase in the magnitude and frequency of extreme temperature and precipitation events (Walsh et al., 2024).

Southern Alaska is characterized by the presence of permafrost (see Fig. 3d). However, in the coastal regions, permafrost is either absent at lower elevations or occurs in isolated and sporadic patches. This is due to the comparatively warmer and more humid climate. More continuous permafrost is found in the inland areas and higher elevations, including the northern Wrangell and Talkeetna mountains (Brown et al., 1997; Obu et al., 2018, 2019).

Due to the mountainous topography, the pronounced seismicity and the coastal geomorphology characterized by numerous fjords, southern Alaska is highly exposed to tsunamis triggered by landslides. A notable example is the 1958 landslide in Lituya Bay, which caused two fatalities due to a tsunami with a run-up height exceeding 500 meters (Miller, 1960). Other reported landslide-triggered tsunamis include those near Grewingk Glacier

in Kachemak Bay in 1967 (Lemaire et al., 2024; Wiles & Calkin, 1992) and in Taan Fjord in 2015 (Haeussler et al., 2018; Higman et al., 2018). Furthermore, tsunamigenic potential has been identified for additional landslides in the Prince William Sound region of south-central Alaska (Schaefer et al., 2024).

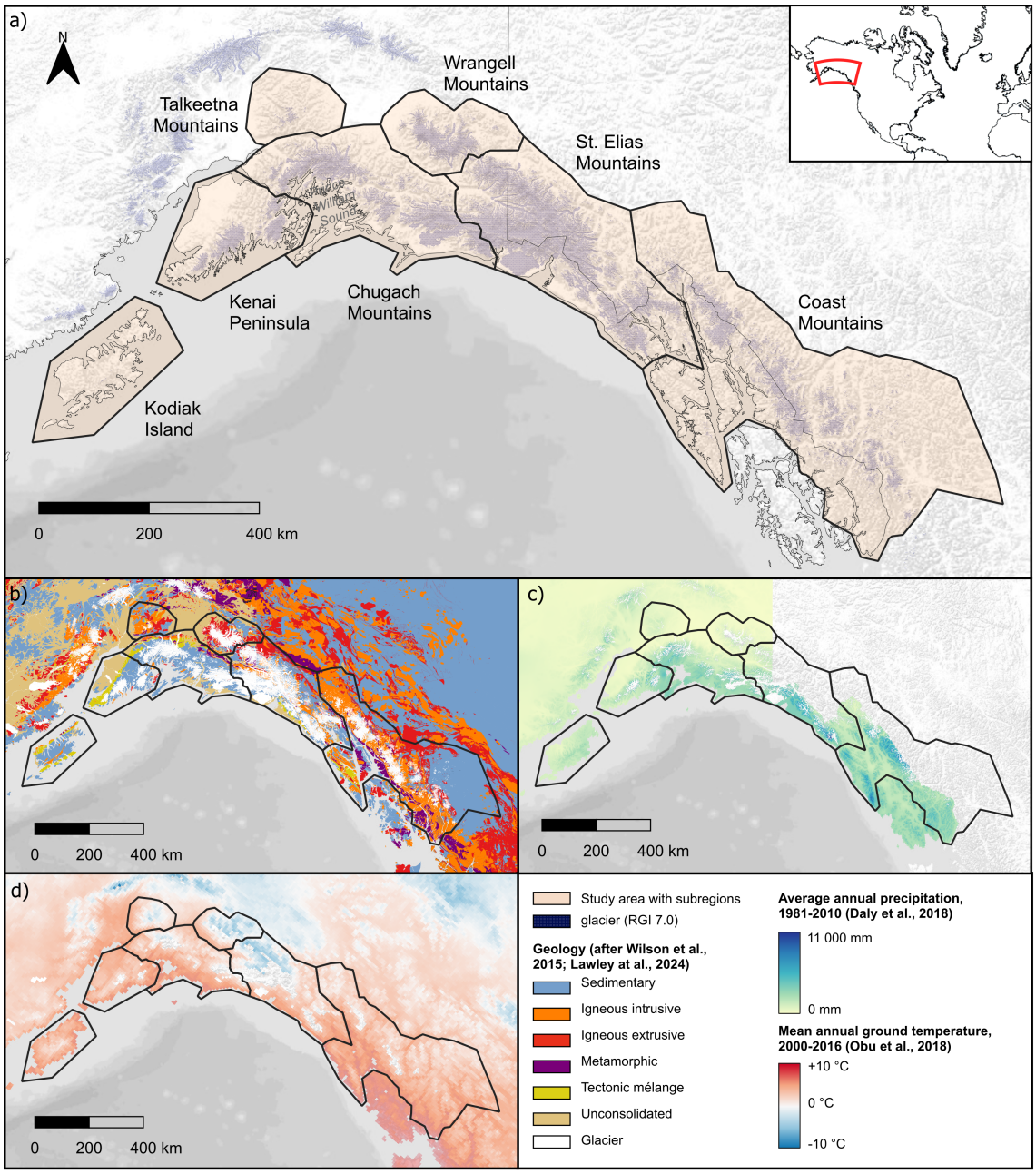

Figure 3: a) General overview of the study area, b) overview of the lithology according to Lawley et al. (2024) and Wilson et al. (2015), c) 1981-2010 annual precipitation (Daly et al., 2018), and d) 2000-2016 Mean Annual Ground Temperature (MAGT) (Obu et al., 2018), Basemap: ESRI World Terrain

4. Data

Table 1: Overview of the utilized data

Source	Data	Use
ITS_LIVE regional glacier and ice sheet surface velocities, version 2 (Gardner, Fahnstock, & Scambos, 2024)	2014–2022 composite surface velocity magnitude and directional components	Landslide mapping (detection) & CNN input
ArcticDEM (Porter et al., 2023b)	10 m mosaic	CNN input
	2 m mosaic	Landslide topography analysis
	2 m mosaic hillshade and slope map	Landslide mapping (confirmation, delineation)
Alaska State high resolution imagery (Maxar Technologies et al., 2020)	True color imagery	
ESRI World Imagery (Esri et al., 2024)		
Planet monthly basemaps (Planet Labs, 2024)	Monthly true color composites (2016 – 2024)	
Global seasonal sentinel-1 interferometric coherence and backscatter dataset (Kellndorfer et al., 2022a)	12-day median VV-coherence (Sep. - Nov.)	Landslide mapping (confirmation)
Sentinel-2 quarterly cloudless mosaics (ESA, 2024)	Seasonal mosaic (Jul. - Sep., 2022) Bands 2, 3, & 4 (Blue, Green, Red)	Landslide mapping (delineation)
	Seasonal mosaic (Jul. - Sep., 2022) Bands 2, 3, 4 & 8 (Blue, Green, Red, NIR)	CNN input
Randolph Glacier Inventory (RGI Consortium, 2017, 2023)	RGI region 1 version 6.0 glacier outlines	Analysis of landslide occurrence in relation to glacier surface elevation change
	RGI region 1 version 7.0 glacier outlines	Landslide mapping (detection), CNN input & analysis of landslide occurrence in relation to precipitation
Regional glacier elevation change time series (Hugonnet et al., 2021)	Annual glacier surface elevation change	Analysis of landslide occurrence in relation to glacier surface elevation change
PRISM climate dataset (Daly et al., 2018)	Alaska 1981–2010 mean annual precipitation	Analysis of landslide occurrence in relation to precipitation
Geologic map of Alaska (Wilson et al., 2015)	Non-generalized geologic units	Geologic characterization of landslides
Canada geologic map compilation (Lawley et al., 2024)	Compiled geological units	
Ground temperature map, 2000-2016, Northern Hemisphere permafrost (Obu et al., 2018)	Mean annual ground temperature, permafrost probability fraction (1 km)	Mean annual ground temperature and permafrost analysis of landslides

4.1. Surface movement

4.1.1. ITS_LIVE regional glacier and ice sheet surface velocities

Data provided by the NASA MEaSUREs Inter-Mission Time Series of Land Ice Velocity and Elevation (ITS_LIVE) project (Gardner, Fahnstock, & Scambos, 2024) offers distributed estimates of glacier surface velocities for all major glaciated regions worldwide. These estimates cover the years 1985 to present and are derived from Sentinel-1 and Sentinel-2, as well as Landsat 4, 5, 7, 8, and 9 imagery, processed using the auto-RIFT feature tracking algorithm (Gardner et al., 2018; Lei et al., 2021). The dataset includes surface velocities of both glaciated and adjacent non-glaciated areas as it stretches 25 km beyond glacier margins.

A composite of average yearly surface velocity estimates between 2014 and 2022, generated using error-weighted least squares fitting, is additionally provided. This time-averaged composite was used for manual landslide mapping and served as input in the CNN-driven landslide detection. Coverage and velocity error are improved from 2014 onward due to the use of Landsat 8 imagery after its launch, resulting in this product being a composite of the years of good data quality.

Data is available in raster format at a 120-meter resolution, encompassing absolute velocity estimates and velocity components in the x and y directions, along with associated error estimates. These error estimates combine uncertainties from natural variability with an estimated systematic error component according to the specific co-registration correction method applied to a grid cell. The error estimates should be interpreted as relative measures of data reliability rather than precise uncertainty quantification (Gardner, Fahnstock, Greene, et al., 2024).

4.1.2. Sentinel-1 interferometric coherence

For confirmation of manually detected landslides, this study utilized data from the Global Seasonal Sentinel-1 Interferometric Coherence and Backscatter Dataset (Kellndorfer et al., 2022a). This dataset comprises radar coherence values derived from Sentinel-1 C-band SAR images collected between December 1, 2019, and November 30, 2020. It provides median repeat-pass coherence values for four seasonal periods December–February, March–May, June–August, and September–November at intervals of 6, 12, 18, 24, 36, and 48 days, using either VV- or HH-polarization. It was chosen because of its broad spatial coverage and accessibility.

In this study, the 12-day median VV-polarization product for the period September to November was chosen because it was the only observation period/polarization product providing complete coverage of the study area. Other seasonal products exhibited noticeably higher decorrelation in mountainous regions, likely due to the presence of snow cover. The dataset was accessed via a REST API (Kellndorfer et al., 2022b).

4.2. Elevation

4.2.1. ArcticDEM

The ArcticDEM digital surface model (Porter et al., 2023b) was used for landslide confirmation and instability polygon delineation in manual mapping, for topographic analysis of the manually detected landslides, and as input channel to the CNN. The dataset was chosen for its high resolution (2 m), which facilitates the identification of small-scale topographic features. Hillshade and slope map visualizations, accessed via a REST API (Porter et al., 2023c) were used for manual mapping. For analysis, the product was accessed through the Google Earth Engine Data Catalog (Porter et al., 2023a) to minimize data download overhead. Additionally, to generate input for the neural network, 10-meter resolution mosaic tiles were accessed via the Polar Geospatial Center.

The product covers regions north of 60° N latitude, with additional coverage, including the entirety of Alaska, but excluding a small part of the study area located south of 60° N and outside the tiles covering Alaska and regions near the border. The elevation data consists of composites derived photogrammetrically from stereo imagery strips collected between 2007 and 2022. Horizontal and elevation accuracies are both approximately 4 m. Despite the application of automated filtering, the dataset still contains uncorrected voids and artifacts caused by atmospheric and environmental conditions such as clouds, fog, shadows, water, and vegetation.

4.3. Multispectral satellite imagery

4.3.1. Sentinel-2 quarterly mosaics

Quarterly cloud-free Sentinel-2 mosaics (ESA, 2024) were used for manual mapping, and as input for the CNN. The red, green, and blue bands were used to delineate instability polygons, while the red, green, blue and near infrared bands were used as inputs to the CNN. This dataset was chosen for its extensive coverage, availability for offline use and its homogeneous data quality. Further, its resolution of 10 m is sufficient to distinguish many landslide characteristics clearly without overly increasing computational load in preprocessing or CNN input size. The third quarter of 2022 (July–September) was selected for its minimal snow cover and its temporal overlap with other datasets, particularly ITS_LIVE. Notably, 2022 marks the final year of the observation period for the utilized ITS_LIVE composite, making the geomorphological features identified in imagery from this year most likely to capture the complete surface movement history within the ITS_LIVE observation period.

The dataset is derived from Sentinel-2 imagery and provides nearly cloud-free mosaics. The digital values in the dataset represent scaled bottom-of-the-atmosphere reflectance (level L2A). The geolocation accuracy of the imagery is unspecified but agreed well with the other utilized data.

4.3.2. World Imagery

The World Imagery (Esri et al., 2024) dataset was used for landslide confirmation and landslide polygon delineation in manual mapping. It is a true color composite derived from multiple sources, with all tiles relevant to the study area sourced from Maxar Vivid imagery, providing a spatial resolution of 0.5 m and a spatial accuracy of 5 m. It was chosen for its high resolution, extensive coverage of Alaska and beyond, and accessibility. The acquisition dates of the imagery relevant within the study area range from 2011 to 2023, although most of the relevant tiles were acquired between 2018 and 2023. The dataset includes some areas affected by cloud cover, shading, and seasonal snow cover.

4.3.3. Alaska State high-resolution RGB imagery

The Alaska State High-Resolution RGB Imagery (Maxar Technologies et al., 2020) was used for the same purposes as World Imagery, to complement it in areas where data quality was poor. This dataset was selected for its high resolution and reliable coverage. It is a true color composite derived from Maxar satellite imagery, similar to World Imagery, providing a spatial resolution of 0.5 m and a spatial accuracy of 5 m. The exact date of image acquisition is unspecified, but based on comparisons with other optical imagery, it is assumed to be within a few years of the publication date (2020). Like World Imagery, this dataset includes areas affected by cloud cover, shading, and seasonal snow cover. However, it often provided clearer imagery in regions where World Imagery data quality was poor.

4.3.4. Planet basemap time series

Planet Basemap true color composite imagery (Planet Labs, 2024) was used to comfirm surface movement in manual mapping. The data, derived from PlanetScope and RapidEye satellite imagery, provide global coverage between 74° N and 60° S, encompassing the entire study area. Monthly composites, available from 2016 to present, are composed to reduce cloud cover, haze, and topographic effects. Composites from August and September were primarily used due to minimal snow cover during these months. Resolution of the imagery scales trigonometrically with latitude, being around 2.2 to 2.8 m within the study area. Spatial accuracy estimates are unavailable, but close spatial agreement with the other used satellite imagery was observed.

4.4. Environmental data

4.4.1. Randolph Glacier Inventory

The Randolph Glacier Inventory (RGI Consortium, 2017, 2023) was used in manual mapping, for masking glaciated areas from non-glaciated areas in precipitation analysis, and as input to the CNN. The RGI is a global inventory of glacier outlines derived from the Global Land Ice Measurements from Space (GLIMS) project, including glaciers larger than 0.01 km^2, with outlines observed around the year 2000. It is structured to distinguish

individual glaciers. It was chosen for its its high quality and coverage of the entire study area.

To analyze landslide distribution in relation to glacier surface elevation change, RGI version 6.0 was used, as it aligns with the glacier elevation change dataset from Hugonnet et al. (2021). In contrast, RGI version 7.0 was used for landslide mapping, precipitation analysis, and as input to the CNN due to its improved data quality. However, differences between the two inventories were found to be minimal in the study area.

4.4.2. Glacier surface elevation change

The glacier surface elevation change dataset of Hugonnet et al. (2021) was used to quantify glacier mass loss. It provides surface elevation changes averaged for the entire glacier surface area for nearly all glaciers worldwide from 2000 to 2019, with glacier distinctions matching those of RGI version 6.0. The data was derived by differencing of DEMs, primarily derived from ASTER satellite imagery. Here, annual averaged elevation change series were used.

4.4.3. PRISM distributed average annual precipitation

Distributed average annual precipitation for the 1981-2010 climatic period (Daly et al., 2018), generated using the Parameter-elevation Relationships on Independent Slopes Model (PRISM), was used for precipitation analysis of the manually mapped landslides. Despite the fact that the climate period does not overlap with that of most other data, including the ITS_LIVE velocity composite (2014-2022), and does not offer coverage of the Canadian parts of the study area, it was prioritized over other temporally closer options. This decision was based on the dataset's high spatial resolution (800 m) and its explicit representation of topographic effects, which are critical in the mountainous study area. The data is derived through interpolation of meteorological station observations, weighted by physiographic factors such as location, elevation, coastal proximity, topographic facet orientation, and others (Daly et al., 2018).

4.4.4. Mean annual ground temperature and permafrost probability

To analyze the relevance of permafrost at the mapped landslide sites, the permafrost extent and ground temperature map for the Northern Hemisphere (Obu et al., 2018, 2019) was used. This dataset was selected due to its relevant time frame (2000-2016), comprehensive coverage of the study area, good spatial resolution, and its inclusion of uncertainty quantification. It was generated by combining remotely sensed land surface temperatures, climate reanalysis, and land cover classification, while accounting for seasonal snow and land cover effects. The dataset provides Mean Annual Ground Temperature (MAGT) at a spatial resolution of 1 km^2, derived from an ensemble of model runs of a temperature at the top of permafrost model. The permafrost probability is additionally provided, defined as the proportion of model runs yielding a MAGT below 0 °C. The dataset has been validated against borehole data, with a reported RMSE of 2.0 °C.

4.4.5. Lithology

The geologic map of Alaska (Wilson et al., 2015) was used to characterize the general lithology of the mapped landslides. It was chosen due to its coverage of the entirety of Alaska, its digital availability and its consistent representation. However, the consistent representation has its limits because as a composite map, it combines various geologic maps with different mapping paradigms, scales, and underlying levels of geologic knowledge developed over more than a century. Units are classified by genesis. Despite extensive integration, inconsistencies and conflicting interpretations persist in the map. The digital version, utilized in this study, offers a reduced degree of spatial and geological generalization compared to the printed map.

To characterize landslides mapped outside the state boundaries of Alaska, the Canadian geological map compilation (Lawley et al., 2024) was used. This map was selected as it offers a generalized geological framework, also referring to the genetic classification of rock units. Some areas are classified into several different lithology categories depending on the source maps, with each classification assigned a confidence category.

5. Methods

5.1. Manual landslide mapping

5.1.1. Manual landslide detection

For detection of landslides in the ITS_LIVE 2014-2022 composite velocity data, the entire study area was manually inspected. In the first iteration, non-glaciated areas with velocities noticeably higher than their surroundings were identified. RGI iventory glacier outlines were used to mask out the glaciated areas. While no strict velocity threshold was set, the data visualization was configured to reduce the distinction of values below 0.1 m a^{-1}. Areas of velocities below 0.1 a^{-1}, which were not particularly extensive, received less attention, as these were within the observed error range for terrain assumed to be stable, consistent with previous inspections of the data for the European Alps.

In a second iteration, the identified pixel patches were assessed to determine whether they represented landslides using auxiliary high resolution true color composite imagery, and hill shades. This data was manually examined for geomorphological features indicative of slope movement, including crowns, crown cracks, scarps, transverse cracks, ridges, deposits, talus, and erosional surfaces (see Fig. 4). Identified sites were only preserved if such evidence was present.

In a third iteration, the temporal evolution of the identified sites was assessed using time-series data of Planet imagery, available for the years 2016 to 2022 and Sentinel-1 coherence. Initial detections that neither showed movement in the time series, nor coherence loss in comparison to their surroundings (see Fig. 4) were only preserved if their appearance in the ITS_LIVE surface velocity data was clear regarding both the velocity magnitudes and the velocity direction and at the same time geomorphological features indicative of slope movement were identified with high confidence. If active movement could be confirmed using time series, high movement confidence was assigned, if it could only be confirmed with coherence loss, considerable movement confidence was assigned, and if it could only be confirmed using ITS_LIVE itself and geomorphological features moderate movement confidence was assigned. Sites that did not meet the criteria for at least moderate movement confidence were excluded from the further mapping and analysis but were retained as preliminary detections of low confidence.

To satisfy the criteria for plausible paraglacial conditioning within recent timeframes, landslides on slopes that were neither glaciated nor showed trimlines — thought to be from the Little Ice Age (LIA) due to minimal overprinting — were excluded from further analysis. Where available, trimlines mapped by Reinthaler and Paul (2023) helped inform this decision. The assumption was that slopes with recent or current glaciation had undergone some degree of paraglacial conditioning. Assumptions about the paraglacial nature of landslides relying on remotely sensed data are challenging and include subjectivity. Consequently, a more conservative approach was adopted, leading to the exclusion of landslides where trimlines were only identified with low or moderate confidence. Nevertheless, for the majority of landslides, the level of uncertainty was minimal, as they were predominantly situated in regions characterized by current glaciation.

5.1.2. Landslide polygon delineation

The delineation of landslide polygons was done using Sentinel-2 quarterly summer (Jul. - Sep.) mosaics from 2022. Summer imagery was selected due to minimal snow cover. Even though other imagery has higher resolution, Sentinel-2 imagery was chosen over other imagery, since it was also used as an input channel in the CNN, and that way alignment of input data and ground truth landslide annotations could be guaranteed. Where Sentinel quarterly mosaics were inadequate due to issues such as low resolution, snow cover, shadows, artifacts, or data gaps, alternative true color imagery was used (see Table 1), depending on their relative clarity for the area.

Instability polygons were delineated at a mapping scale of 1:5000. The goal was to include the entire area affected by the landslide into the polygon, and not just active areas. On the one hand, this avoids ambiguities in determining active parts, on the other hand it increases the information amount for the use of the polygons in the CNN. The upper boundary was delineated at the landslide crown. In cases where they were visible, crown cracks were also included in the instability polygon. The lower boundary traces the landslide toe. Lateral boundaries are drawn tracing the landslide flank or along lateral shear zones where visible. Where lateral shear zones were indiscernible, lateral boundaries were approximated using destabilized areas identified from ITS_LIVE surface velocity data.

A confidence level was assigned to each delineated polygon based on the clarity of its boundaries:

- Medium confidence: Assigned when the proposed upper, lower, and lateral boundaries of the instability area could be identified with reasonable confidence.
- Moderately low confidence: Applied when any parts of the instability area boundary were ambiguous. This included cases such as:
  - Unclear lateral delineation of slope areas affected by movement (most common)
  - Landslides with indistinct crown cracks
  - Landslide toes blending into supraglacial debris
- Low Confidence: Assigned when more than one of the above criteria for medium confidence applied.

5.1.3. Topographic characterization of the landslides

Topographic parameters were calculated to characterize the topography of the mapped landslides. This serves a dual purpose: It may indicate detection biases that are dependent on elevation, slope or aspect, but may also be informative about physical factors of slope destabilization.

The ArcticDEM at a 2-meter resolution was used for topographic characterization. For better accuracy of the absolute elevations, elevation values were corrected from geoid height to mean sea level height. The mean elevation within the instability polygons was computed using area-weighted average.

To calculate the mean slope gradient and aspect, the DEM was resampled to a lower 10 m resolution to reduce the influence of small-scale geomorphological features, such as boulders or cracks, which do not represent the overall slope gradient or aspect of the landslides. The average slope and aspect of the landslides were then calculated by deriving slope and aspect maps from the resampled DSM and computing the area-weighted averages within the landslide polygons.

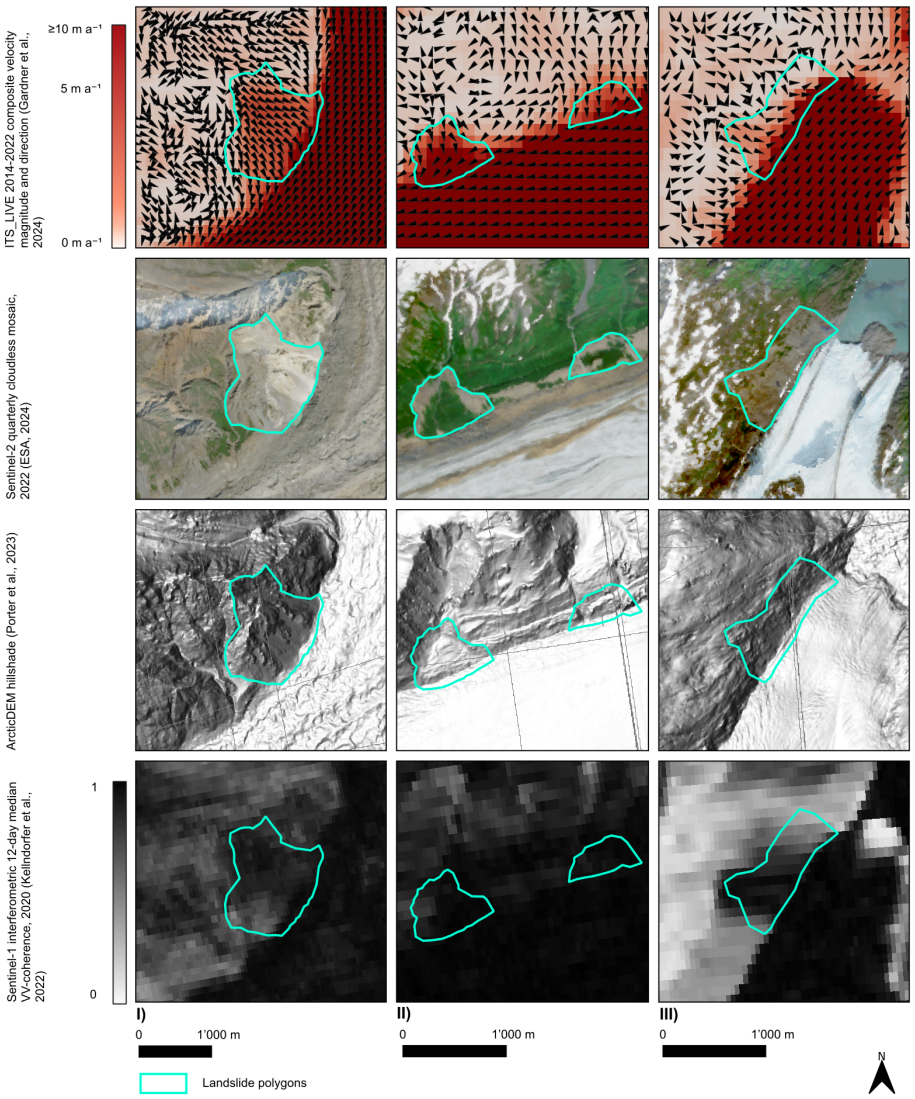

Figure 4: Examples of 3 landslides, demonstrating situations encountered in mapping, in different datasets. I) clear ITS_LIVE velocity components; low delineation confidence, as delineation is unclear on all sides; longitudinal faults and scarps visible in image and DEM; some coherence loss, II) ITS_LIVE pixel mixing at glacier margin; moderately low delineation confidence as lateral delineation is unclear; scarps, crowns and foot visible in satellite imagery; crowns, scarps, transverse ridges, foot and cracks visible in DEM; coherence loss only on the western landslide; landslides in unconsolidated surficial deposits, III) ITS_LIVE pixel mixing at the glacier margin; medium delineation confidence; scarps, crown, shear zones and foot visible in satellite imagery and DEM; clear coherence loss.

5.2. Landslide detection using Mask R-CNN

5.2.1. Model architecture

Mask R-CNN (Region-based Convolutional Neural Network) is a deep learning framework for instance object detection, object classification and instance segmentation in images, introduced by (He et al., 2017). This specific model was chosen because of its adaptability, usability and good performance in other landslide detection tasks (e.g., Fu et al., 2022; Liu et al., 2022; Ullo et al., 2021). In this study, the Mask R-CNN implementation provided by Abdulla (2017) was utilized, with adjustments from Mahmud (2024) to ensure compatibility of dependencies with the environment on the virtual machines used for model training.

The architecture of Mask R-CNN consists of several components (see Fig. 5). First, a convolutional neural network acts as the backbone used to extract feature maps. The backbone network is combined with a Feature Pyramid Network (FPN), which generates and combines feature maps at different resolutions to improve subsequent object detection and segmentation at different scales. A ResNet-101 (He et al., 2015) backbone, which features 347 layers, was used in this study, as it was found to perform well compared to a less deep alternative in a landslide detection study by Ullo et al. (2021).

The Region Proposal Network (RPN) in Mask R-CNN proposes rectangular anchor boxes of different sizes and aspect ratios based on the feature maps generated by the backbone network. Proposals redundant due to overlap are filtered, providing the final set of region proposals for further processing. The proposal boxes are fed into two separate layers, one of which further refines the region proposals to better fit the extent of the proposed objects and the other classifies the proposals into background (no object present) or foreground (object present). The feature maps from which the region proposals are derived are at a lower resolution than the input tiles. The ROIAlign module precisely maps the region proposals to the resolution of the input tiles (He et al., 2015; Ren et al., 2016).

The aligned region proposals are passed on to the head component of the network, which consistes of three branches: The bounding box branch refines the bounding box of the object by determining shifts and scaling factors of the bounding box using fully connected layers. The classification branch computes the likelihood of different object classes (in this study only background and landslide) using fully connected layers and a softmax output. While these two tasks are already performed in the RPN, they are refined on the basis of the proposals aligned by ROIAlign. Finally, the mask branch uses a fully convolutional network to generate pixel-wise binary masks, which are scaled to the input tile size to draw boundaries of the detected objects.

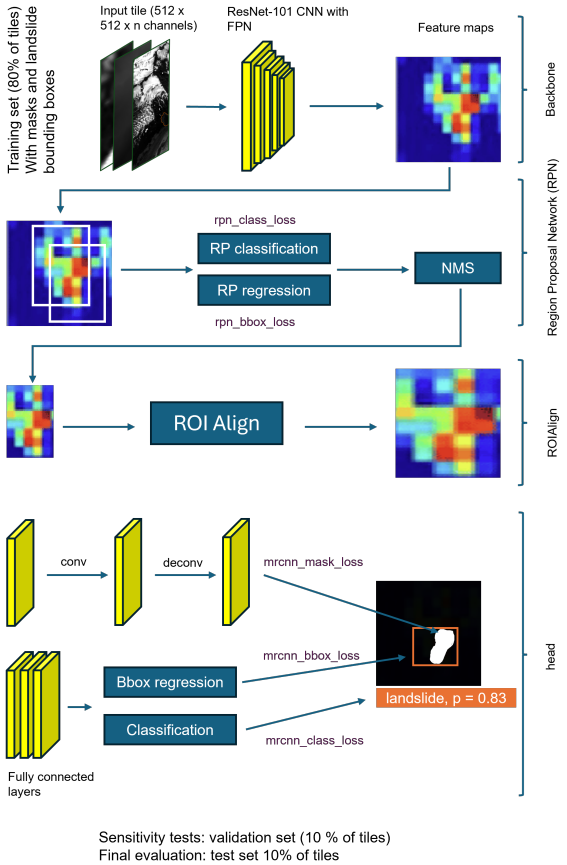

Figure 5: Overview of the model architecture, including the losses, and the training process. Feature map illustration taken from Zhang et al. (2020).

5.2.2. Input data selection

Different spatial information can be passed on to the model in gridded form as separate channels of the same tile. The selection of input data additional to ITS_LIVE surface velocities was guided by the goal of matching the most informative datasets in manual mapping and by literature suggestions, which demonstrated the value of the use of DEMS and multispectral imagery (e.g., Ghorbanzadeh et al., 2019; Nava et al., 2021, 2022), as well as categoric data descriptive of environmental features (Liu et al., 2021; Shi et al., 2021) for landslide detection.

Following the aim of the project, the ITS_LIVE composite velocity magnitudes were a central input channel. Manual mapping revealed the corresponding movement directions to be valuable in detection of slope movements, which is why the x- and y components of the ITS_LIVE composite were also included in the selection. The ArcticDEM was selected to enable the model to derive information on slope characteristics, as well as to provide information about geomophological features indicative of landslides. As multispectral imagery played a crucial role in confirmation of slope movements and delineation of their perimeters, Sentinel-2 quarterly mosaic imagery was chosen as an input channel. All channels available in the Sentinel-2 seasonal mosaics (R, G, B, NIR) were included. Lastly,

rasterized RGI 7.0 glacier polygons were chosen as they provided value in preventing misclassification of small glaciers and debris-covered ice as landslides in manual mapping.

5.2.3. Input data preparation

The input tile size to neural networks is constrained by computing memory. Thus, large geospatial datasets must be split into smaller tiles. When using imagery from different sources as separate channels, this imagery must be resampled to precise alignment. Further, normalization of pixel values needs to be performed to help mitigate biases, and improve model stability.

An exact 10 m resolution grid in the Alaska Albers projection was defined for all input channels. ITS_LIVE velocity data, originally at 120 m resolution, was reprojected and upsampled using bilinear interpolation. An additional correction was applied to the velocity directions to directly adjust the azimuths for angular distortions. These distortions occurred because the velocity components were originally calculated from the NSIDC Sea Ice Polar Stereographic North projection. The correction ensured that not only the spatial alignment but also the velocity directions encoded in the pixel values account for the distortions introduced by reprojection. The arcticDEM and Sentinel-2 imagery, which originally already had a 10 m resolution, were reprojected and resampled to match the predefined grid. Finally, RGI glacier polygons were rasterized to match to the same grid.

ITS_LIVE velocity magnitudes were normalized to a [0, 1] scale, with 0 corresponding to 0 m a^{-1} and 1 corresponding to 10 m a^{-1}. This approach effectively represented surface velocities within landslide areas (only one landslide polygon had a median velocity exceeding this threshold), while minimizing the influence of extreme high-velocity pixels on the data range. To account for the circular nature of the azimuth of the velocity direction, the directions were transformed to Cartesian coordinates and split into two channels, with one representing the sine, and the other the cosine component in a range [-1, 1]. The ArcticDEM was normalized to a [0, 1] range using min-max normalization to retain the meaningful interpretation of topography. Sentinel imagery was normalized to the same range using quantile normalization, with the 0.02 and 0.98 quantiles for each channel. This provided a balance between preserving most pixel values while reducing the impact of extremely low and high values. The rasterized RGI polygons were assigned binary values, with 1 representing glaciers and 0 indicating non-glaciated areas. To denote missing data, a value of -2, which falls outside the normalization range, was used for all channels.

For tiling of the input data, a tile size of 512 x 512 pixels was chosen, corresponding to an area of 26.2 km^2 per tile. Square tile sizes, with power of two dimension, ensure compatibility with the model architecture and improve computational efficiency. Tiling was applied for all areas with data coverage by ITS_LIVE within the study area. A tile overlap of 48 pixels was used. The overlap helps to prevent the loss of important information at the edges of tiles. Still, tiling can lead to some objects being cut off and partially represented in multiple tiles, and spatial context may be limited near tile boundaries. See Figure 6 for an illustration of the input tiles.

The resulting tile number was high, but imbalanced, with the vast majority containing no landslides. To address this, the dataset size was reduced by only including tiles that

contained mapped landslides, along with an equal number of randomly selected tiles without landslides. Also having tiles without annotated landslides is important, as it ensures the model is trained to recognize and handle areas where landslides are absent, which is needed for generalizing to real-world application scenarios.

The tiles were annotated with metadata specifying their spatial extent. While the model does not consider spatial context beyond pixel coordinates, this metadata allowed for the reestablishment of spatial context after the model's predictions.

Finally, binary raster masks representing the presence or absence of landslides were created. These masks were generated from the manually mapped landslide polygons by rasterizing them to precise alignment with the input channels. Aligning rectangular bounding boxes are automatically derived from the masks when loading the data in the model.

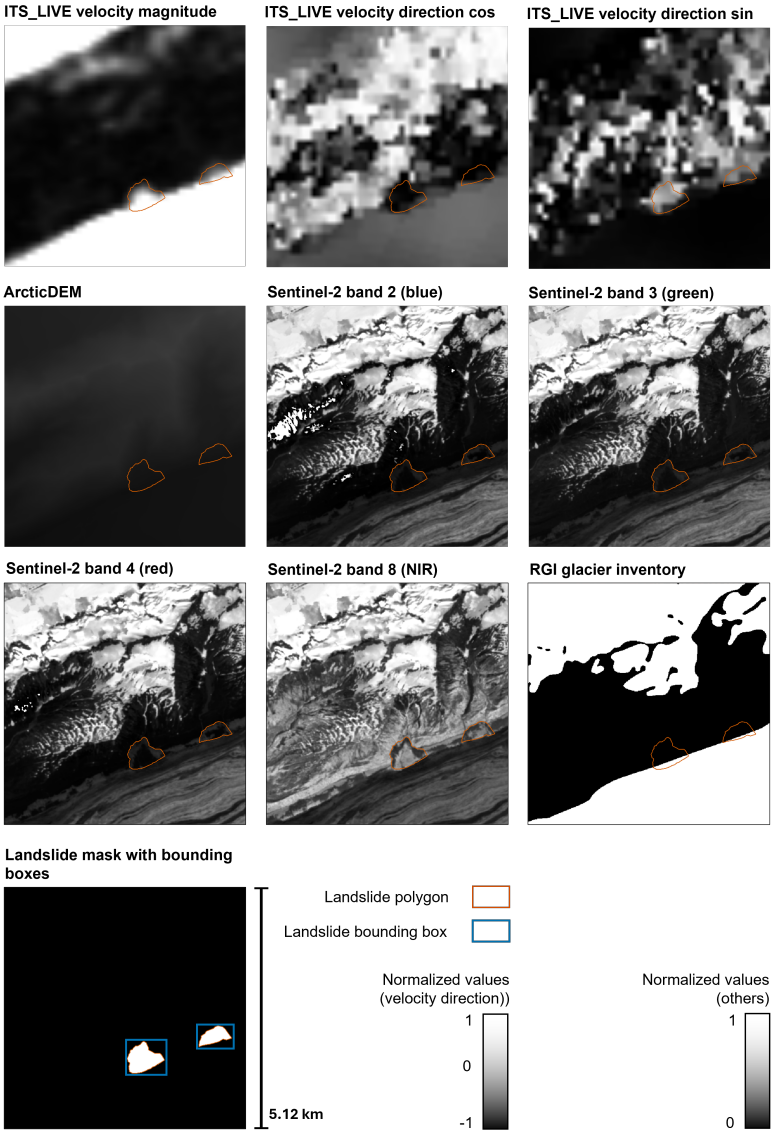

Figure 6: Appearance of the normalized input tiles in all channels, and the corresponding ground truth mask and bounding boxes.

5.2.4. Input data cases

To evaluate the sensitivity of the model to different input channel configurations, the model was trained and assessed using seven distinct configurations.

Configuration case I included all 9 input channels. In case II, the three channels containing ITS_LIVE surface velocity magnitudes and surface velocity directions were excluded. To assess the importance of the directional components, a configuration was defined with velocity magnitudes included but the directional components excluded (case III). Additional configurations were defined as follows: case IV included all channels except ArcticDEM, case V excluded all Sentinel-2 bands, and case VI excluded the RGI inventory (see Table 2).

A further input data case (case VII) was defined to evaluate the sensitivity to data augmentation. Data augmentation are techniques to apply alterations to the input data to artificially enhance the size and diversity of the input dataset. Vertical and horizontal flips, as well as a combination of both, were applied to augment the tiles of the training set, increasing its size by a factor of four. In this case, a configuration that included all input channels except the directional velocity components was used, as the geometric transformations applied to the tiles would misalign the directional information with the other channels.

Table 2: Overview of input data cases, x denotes inclusion.

	Case I	Case II	Case III	Case IV	Case V	Case VI	Case VII
ITS_LIVE velocity magnitudes	x		x	x	x	x	x
ITS_LIVE velocity directions cosine	x			x	x	x	
ITS_LIVE velocity directions sine	x			x	x	x	
ArcticDEM	x	x	x		x	x	x
Sentinel-2 Bd. 2 (Blue)	x	x	x	x		x	x
Sentinel-2 Bd. 3 (Green)	x	x	x	x		x	x
Sentinel-2 Bd. 4 (Red)	x	x	x	x		x	x
Sentinel-2 Bd. 8 (NIR)	x	x	x	x		x	x
RGI 7.0 inventory	x	x	x	x	x		x
Augmentation applied							x

5.2.5. Model training

The dataset consisted of 467 image tiles, half of which contained landslides. This dataset was divided randomly into training, validation, and test splits. 80 % of the tiles were allocated to the training dataset, while the remaining tiles were split equally into the validation dataset and the test dataset.

The training dataset consists of the tiles and their ground truth landslide annotations, which the model uses for training. The validation dataset helps evaluate model performance across training epochs and assess the sensitivity to different input configurations. Although

this data was not directly used for model training, the performance on the validation data was used to guide hyperparameter decisions during model development. Thus, data leakage may have occurred. This means that the model did to some degree indirectly learn from the validation data, and this could lead to overestimated performance metrics. To avoid this issue, a separate test set was used for the final evaluation. The test dataset was only assessed after full training, using the model weights performing best on the validation dataset. This ensures that the final model evaluation is truly independent of data encountered during training.

The model was trained for 125 epochs, with 47 steps per epoch. During each step, 8 images were processed, ensuring that each image was used once per epoch. During training, losses are computed based on the comparison of the predictions and ground truth, based on which model weights are optimized using backpropagation and gradient-descent.

There are different losses for different components of the model. The sum of these components is the total loss that is used to optimize the model weights (see Fig. 5). The RPN classification loss (rpn_class_loss) is based on the successful categorization of the region proposals into foreground and background. The RPN region proposal loss (rpn_bbox_loss) quantifies the quality of the region proposals by comparing the position and extent of the region proposals to the ground truth bounding boxes, but only for the foreground predictions. The head classification loss (mrcnn_class_loss) quantifies the quality for the refined object classifications. The head bounding box loss (mrcnn_bbox_loss) quantifies the quality of the predicted bounding boxes positions and extents compared to the ground truth bounding boxes, and the head mask loss (mrcnn_mask_loss) compares the predicted masks to the ground truth masks. Smooth L1-losses which penalize small errors quadratically and large errors linearly are used for loss calculation of the region proposals and bounding boxes. For the classification and mask losses, cross-entropy is used, which takes into account the confidence of predictions and penalizes stronger if confidence in categorical predictions is high (Abdulla, 2017; He et al., 2017). Losses were additionally computed on the validation dataset for monitoring purposes.

Training was conducted with all weights adjustable. The learning rate was adjusted throughout the epochs to allow for larger weight updates early in training and finer adjustments as training progressed. The learning rate increased linearly from 0 to 0.01 to stabilize initial training, which was followed by a step-wise exponential decay of the learning rate by a factor of 0.5 every 15 epochs. A weight decay of 0.005 was set, higher than the default, to counteract overfitting. The scales of the RPN anchors were set between 24 and 256 and to aspect ratios between 0.25 and 4, reflecting the sizes and form factors of the mapped landslides (see Table 3).

Table 3: Configuration and hyperparameter settings in Mask R-CNN.

Parameter	**Value**
Backbone network	ResNet-101
Number of image channels	5-9, depending on input case
Tile height [pixels]	512
Tile width [pixels]	512
Scales of RPN anchors [pixels]	[24, 32, 64, 128, 256]
Aspect ratios of RPN anchors	[0.25, 0.5, 1, 2, 4]
Number of epochs	125
Steps per epoch	47
Batch size	8
Weight decay	0.005

5.2.6. Evaluation metrics

The model performance was evaluated using the confusion matrix, precision, recall, F1 score and the mean intersection over union (mean IoU). The confusion matrix expresses the number of true positives (TP), false positives (FP), and false negatives (FN). True positives are correctly detected landslides, while false positives are wrongly detected landslides, and false negatives are undetected landslides. Since the model did not do detections of background, true negatives are not defined. If the same landslide was identified by more than one separate prediction, these additional predictions were counted as false positives. A prediction was considered correct if the bounding boxes at least partially overlapped. This is a rather weak criteria, and higher overlaps thresholds could be chosen. However, these criteria are justified with the low confidence in correct landslide polygon delineations, which translate to low confidence in the bounding boxes.

Precision quantifies the proportion of correct detections out of all detections:

$$\text{Precision} = \frac{TP}{TP + FP} \tag{1}$$

Recall quantifies the proportion of correctly detected objects detected out of all detactable objects in the ground truth data.:

$$\text{Recall} = \frac{TP}{TP + FN} \tag{2}$$

The F1 score is a proportional measure of precision and recall, which is defined as:

$$F1 = 2 \times \frac{\text{Precision} \times \text{Recall}}{\text{Precision} + \text{Recall}} \tag{3}$$

The mean IoU quantifies the alignment of the predicted bounding boxes. It is the average of the intersecting areas of bounding boxes of correctly detected objects with the ground truth boxes, divided by the combined areas of those boxes.

5.2.7. Evaluation of sensitivity to different input data cases

To evaluate the model's sensitivity to different input data cases, the weights generated in each epoch of training were assessed against the validation dataset. In addition to the loss values, this provides a clear and interpretable view of how the models' performance evolved across epochs for the different input data cases, providing insights about their impact on the model performance

5.2.8. Final model performance evaluation

To assess the model's final performance, it was evaluated on the test dataset using the best-performing weights from validation. These weights were selected based on the product of the F1-score and mean IoU. This ensured that both a balance of precision and recall, as well as bounding box alignment, are considered. Mask evaluations were not conducted, as the focus is on detection rather than precise segmentation. However, they remain informative for interpreting the results.

5.3. Connections between landslide occurrence and environmental factors

5.3.1. Landslide occurrence in connection to glacier mass loss

To assess the connection between the occurrence of the mapped landslides in relation to glacier mass loss, the Hugonnet et al. (2021) glacier elevation change dataset was used.

Under the assumption that glaciation and deglaciation likely conditioned the slopes of the mapped landslides, the landslides were attributed to specific glaciers. For this attribution, each mapped landslide was assigned to the glacier occupying the slope of the landslide. In some instances, landslides were associated with multiple glaciers following this definition. In these cases, smaller glaciers occupy the upper part of the slope, while larger, faster-moving glaciers occupy the valley bottom. In such cases, the landslides were attributed to the larger, typically faster-moving valley glaciers under the assumption that these glaciers and their development is more relevant for recent slope conditioning.

The mean surface elevation change of each glacier was calculated for the period 2000-2019, which only partially overlaps with the observation period of the velocity data used in landslide mapping (2014-2022). However, to provide a more comprehensive representation of glacier recession, the full time period (2000-2019) of glacier surface elevation change data was used, minimizing the effect of year-to-year variability. This approach also assumes that slope movements active between 2014 and 2022 may have been critically influenced by glacier recession prior to this observation period. For comparison

among the subregions, the area-weighted average glacier surface elevation change was calculated for both the entire study area and the individual regions.

5.3.2. Landslide occurrence in connection to precipitation

For analysis of the occurrence of the mapped landslides in relation to precipitation, the 1981–2010 distributed average annual precipitation data from the PRISM climate dataset Daly et al. (2018) was used.

To contextualize precipitation levels at landslide sites, a statistical comparison was performed between the sites of mapped landslides and sites where no landslides were mapped. To limit comparison to sites with dissimilar topographic conditions and spatial relation to glaciers, the comparison area was restricted to non-glaciated terrain within the study area, ensuring it was no farther from glaciers (using RGI 7.0 outlines) than the 90th percentile distance between landslide polygon centroids and glacier outlines (392 m).

A grid with a resolution matching the PRISM dataset (800 m) was applied to the study area. grid cells fully covered by glacier ice (according to RGI 7.0) were excluded from further analysis. grid cells that intersected with mapped landslide polygons were classified as 'landslide' cells, while those that did not intersect and were within the distance threshold of glacier outlines were classified as 'non-landslide' cells. Each grid cell was assigned the mean annual precipitation from the PRISM dataset. This process resulted in a dataset, containing the average annual precipitation and a binary landslide classifier for each grid cell.

To assess the effect of precipitation (P), on the landslide occurrence, a univariate logistic regression model was fitted:

$$\text{logit}(\pi_{\text{landslide}}) = \beta_0 + \beta_1 P$$

where $\pi_{\text{landslide}}$ is the probability of a landslide occurring, β_0 is the intercept, and β_1 is the effect of precipitation on landslide occurrence. A statistically significant non-zero β_1 coefficient would indicate that average annual precipitation has an effect on landslide occurrence.

5.3.3. Mean annual ground temperature and permafrost probability at the landslide sites

To analyze the relevance of permafrost at the mapped landslide sites, the permafrost extent and ground temperature map for the Northern Hemisphere was used (Obu et al. (2018, 2019). To assess the MAGT and probability of permafrost presence at the location of a mapped landslide, the MAGT and permafrost probability from that dataset were sampled using an area-weighted mean within the landslide polygons.

5.3.4. Lithological characterization of the landslide sites

To assess the general lithology of the mapped landslides, it was inferred from units from the geologic map of Alaska (Wilson et al., 2015). Geologic units were manually assigned because the map's spatial generalization and temporal range, reflecting older glacier extents, would otherwise often misclassify landslide polygons near glacier ice as part of the glacier unit. Where more than one geologic unit intersects with a landslide polygon, the unit is assigned according to the largest overlap. For landslide sites mapped entirely as glacier, the geologic unit adjacent to the glacier margin on the side of the landslide is assigned.

For landslides within Canadian territory not covered by the Alaskan geologic map, the Canada geologic map compilation (Lawley et al., 2024) was used with a similar manual mapping approach. However, in this map, the same area is often mapped as part of different units simultaneously but with different qualitative confidence levels. In these cases, the mapped unit with the highest confidence was given priority.

Although unconsolidated Quaternary surficial deposits are mapped, the mapping scale does not capture their detailed distribution well enough, especially in the case of moraines along present glacier margins. As a result, the general assignment method described above may misclassify instabilities in these deposits. When true color satellite imagery (ESRI World Imaery) clearly showed that a landslide occurred entirely in unconsolidated deposits rather than bedrock, manual reclassification was applied. Landslides in unconsolidated deposits were identified by the absence of stratification and a smooth, homogeneous surface color and texture (see Figure 4). Reclassification was done only if these criteria applied to the entire landslide area.

To simplify interpretation across a large and geologically diverse study area, classifications were generalized into broader categories based on similar lithological properties. These categories are unconsolidated surficial deposits, siliciclastic sediments, chemical sediments, igneous intrusive rocks, igneous extrusive rocks, tectonic mélanges, and mixed metamorphic rocks. The categorization was based on the source maps, except for the distinction between siliciclastic and chemical sediments within Alaska, which was done by the author but referring to textual descriptions in Wilson et al. (2015).

6. Results

6.1. Manually mapped landslides

6.1.1. Overview and distribution of manually mapped landslides

In total 182 landslides were mapped. With most of them (86) in the St.Elias mountains, the Chugach Mountains (41) and the Coast Mountains (37). Fewer were mapped in the Wrangell Mountains (9), the Kenai Peninsula (7) and the Talkeetna Mountains (2). No landslides were found and mapped in the Kodiak Island region (see Figure 7.

Clusters of landslides are found in the coastal eastern part of the Chugach Mountains, the coastal southeastern part of the St. Elias Mountains, and the coastal regions of the Coast Mountains. Areas of fewer landslides were detected in the central Chugach Mountains, the area surrounding the Juneau Icefield, and the central St. Elias Mountains. For detailed examples, refer to Fig. 4).

Of the 182 landslides, movement confidence is high for 155, moderately high for 15 and moderate for 12. The confidence in the delineated landslide polygons was judged to be moderate for 27 instances, somewhat low for 86 instances and low for 69 instances.

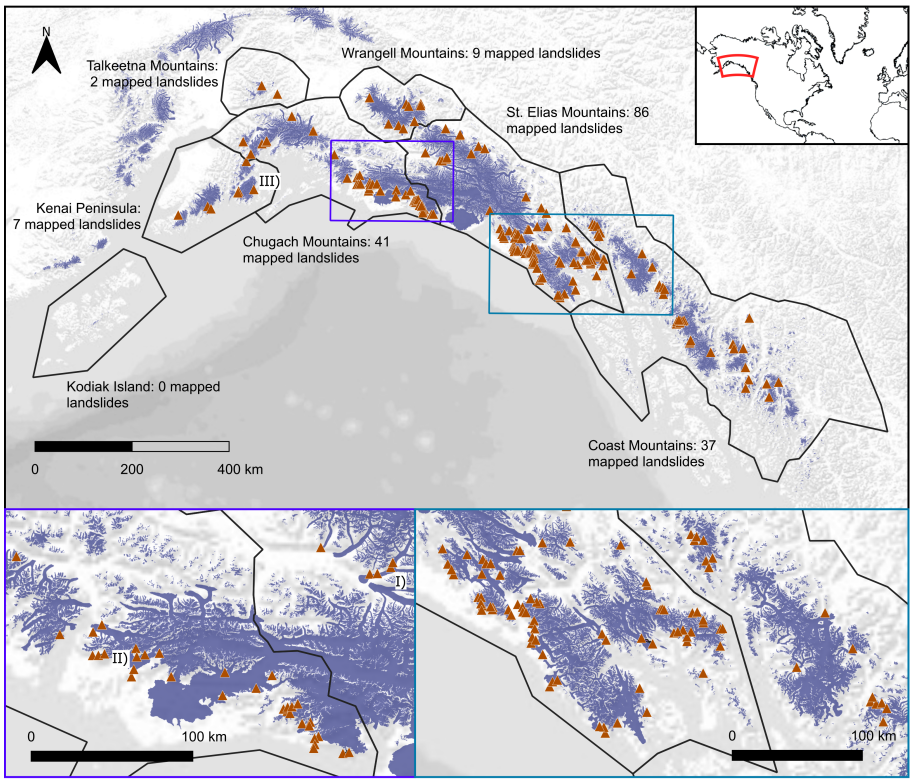

Figure 7: Distribution of the manually mapped landslides. Roman numbers indicate instances shown in more detail in Figure 4

6.1.2. Topographic characterization of mapped landslides

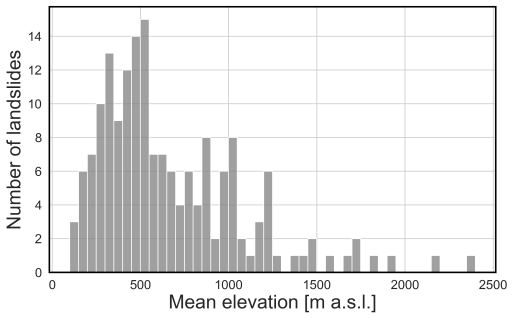

(a) Mean elevation of the mapped landslides

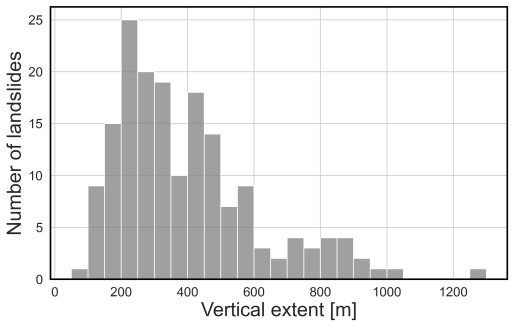

(b) Vertical extent of the mapped landslides

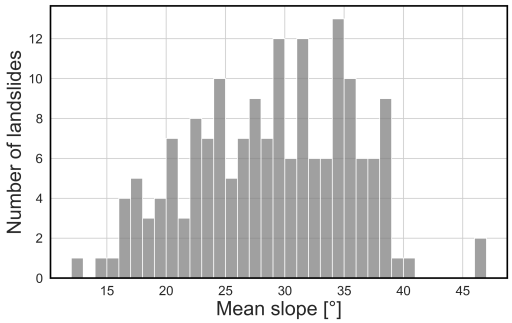

(c) Mean slope of the mapped landslides

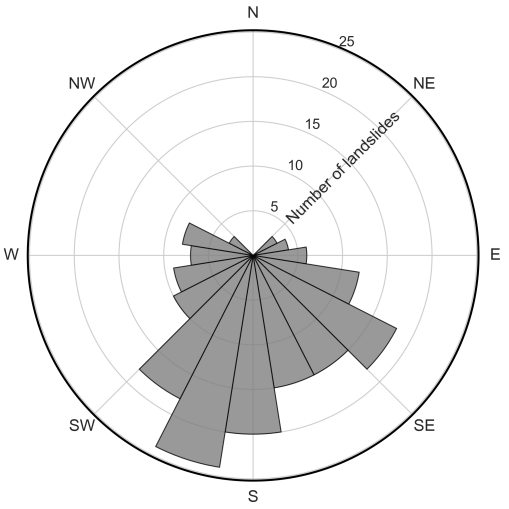

(d) Mean aspect of the mapped landslides

Figure 8: Topographic metrics for the manually mapped landslides

Elevation data was available for 172 of the 182 mapped landslides. For these 172 landslides, the mean elevations span a range from 99 to 2397 m a.s.l., with an average mean elevation of 668 m a.s.l. between landslide areas (see Fig. 8a). The landslide with the smallest vertical extent spans 88 m, while the largest vertical extent is 1277 m (see Figure 8b).

The mean slope of the mapped landslide areas is 28.9°, with slopes ranging from 12.1° to 46.2°. Most landslides occur on slopes between 20° and 40°. South-facing aspects dominate, with the majority of landslides having southwest (SW) to southeast (SE) orientations. In contrast, relatively few landslides have east- or west-facing aspects, and none are north-facing.

Landslide areas range from 50'520 m^2 to 5'019'040 m^2, with a mean of 523'390 and a median of 362'340 m^2.

6.2. Landslide detection using Mask R-CNN

6.2.1. Model training performance

Figure 9 illustrates the evolution of model losses across all training epochs for all seven input data cases, displaying the loss components from each model component as well as the total loss. This indicates how well the overall model and each model component fit the training data, with smaller losses indicating a better fit.

The following key observations are made:

- Training loss follows an exponential decrease in all input data cases.
- Model fitting after 125 epochs is comparably good for cases I to VI with minor variations, but less optimal in case VII.
- Classifications losses contribute only minimally to training loss.
- After earlier epochs of training, loss is dominated by the loss of the region proposals of the RPN, except for case VII where the bounding box loss and mask loss of the head remain clear contributors.

Figure 10 illustrates the same losses assessed on the validation data. This provides information about the model's representation of unseen data, with lower values corresponding to a better fit.

Following are the key observations:

- Validation loss, overall is markedly higher than training loss.
- The classification losses have minimal contribution, while the mask and bounding box loss of the head contribute meaningfully in all cases.
- Initial decrease in validation loss is present in all cases except case VI.
- Increase in validation loss is primarily driven by increases of the region proposals loss of the RPN.
- The increase of the RPN region proposal loss is particularly pronounced if the RGI inventory is excluded.
- Initial decrease of the total loss is more pronounced and later increase is limited in case VII compared to the other cases.

6.2.2. Model sensitivity to input data cases

Figure 11 presents the evaluation metrics for landslide detection (bounding box prediction) assessed on the validation dataset for the seven different input data cases, with results shown across all training epochs. Unlike the model losses discussed in the previous section, these metrics are more interpretable and specifically focus on the bounding box detection task only, disregarding mask prediction and performance of the separate model components (for evolution across the epochs refer to Fig. A.0.1 in the Appendix).

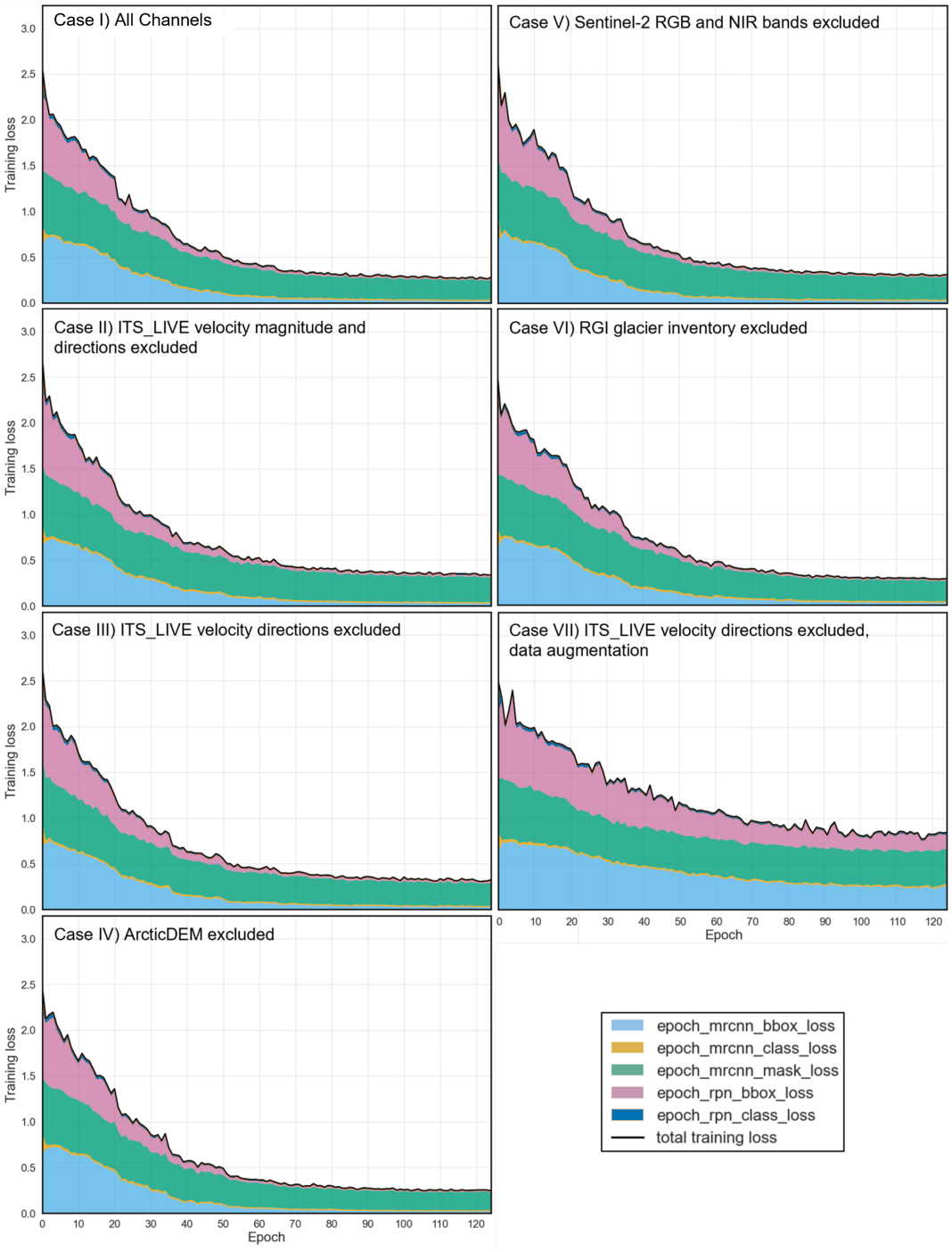

Figure 9: Training loss curves across all epochs for the seven input data cases, reflecting the model representation of the test data, and the performance of the different model components.

Figure 10: Training validation loss curves across all epochs for the seven input data cases, reflecting the model representation of the validation data, and the performance of the different model components.

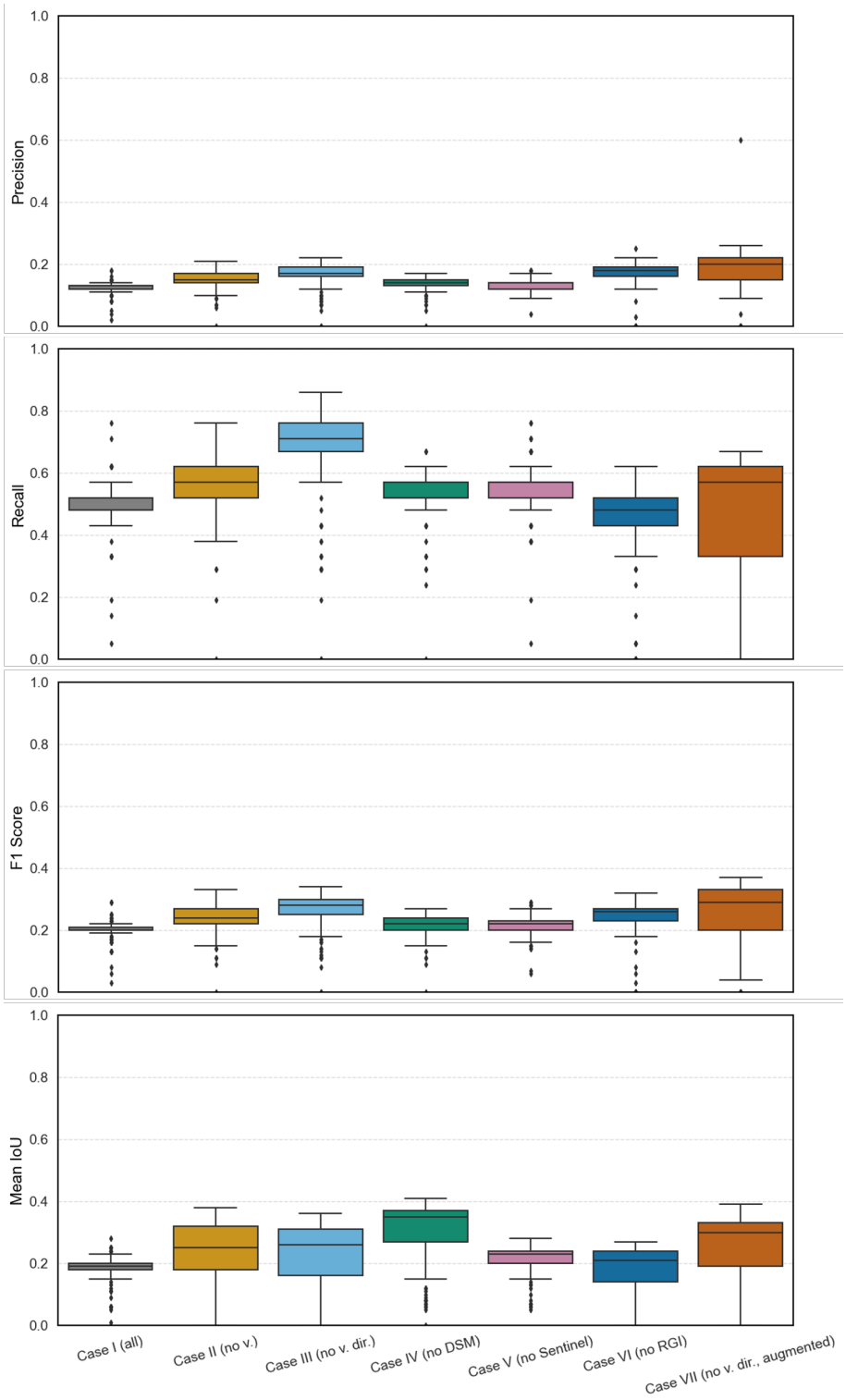

Figure 11: Performance of all training weights in detection of the validation set for all input data cases.

The following observations relating to the different performance of the input data cases can be made:

1. Performance is poorest with the inclusion of all input channels, and omission of any input layer leads to gains in detection performance.
2. Omission of only ITS_LIVE velocity directions offers improvements in comparison to omission of velocity magnitudes and directions combined, resulting in the best model performance without application of data augmentation.
3. Omission of the DEM or Sentinel-2 data results in worse performance than omission of ITS_LIVE data.
4. Despite poor precision and recall, omission of the DEM leads to comparatively good bounding box alignment, while omission of Sentinel-2 leads to comparatively poor bounding box alignment.
5. Omission of the RGI inventory results in comparatively high precision but low recall and poor bounding box alignment.
6. Data augmentation helps improve the balance of precision and recall, while also improving bounding box alignment (compare case VII and case III).

6.2.3. Final model performance

Table 4: Model performance of the best performing weights on the validation dataset evaluated on the test dataset.

Metric	Precision	Recall	F1 Score	Mean IoU
Validation	0.25	0.67	0.36	0.35
Test	0.20	0.53	0.29	0.34

The input data case and training epoch combination with the best performance on the validation dataset, was epoch 72 of case VII (velocity directions left out, data augmentation applied). Using these weights for landslide detection (bounding box prediction) on the test dataset results in a precision of 0.2, meaning the ratio of true positives to false positives is 1:4. The recall is 0.53, meaning 53 % of the landslides in the ground truth data were detected, and the mean IoU is 0.34, which means that the mean overlapping area of predicted and ground truth bounding boxes is 34 % of the total area covered by both.

6.3. Connections between landslide occurrence and environmental factors

6.3.1. Landslide occurrence in relation to glacier mass loss

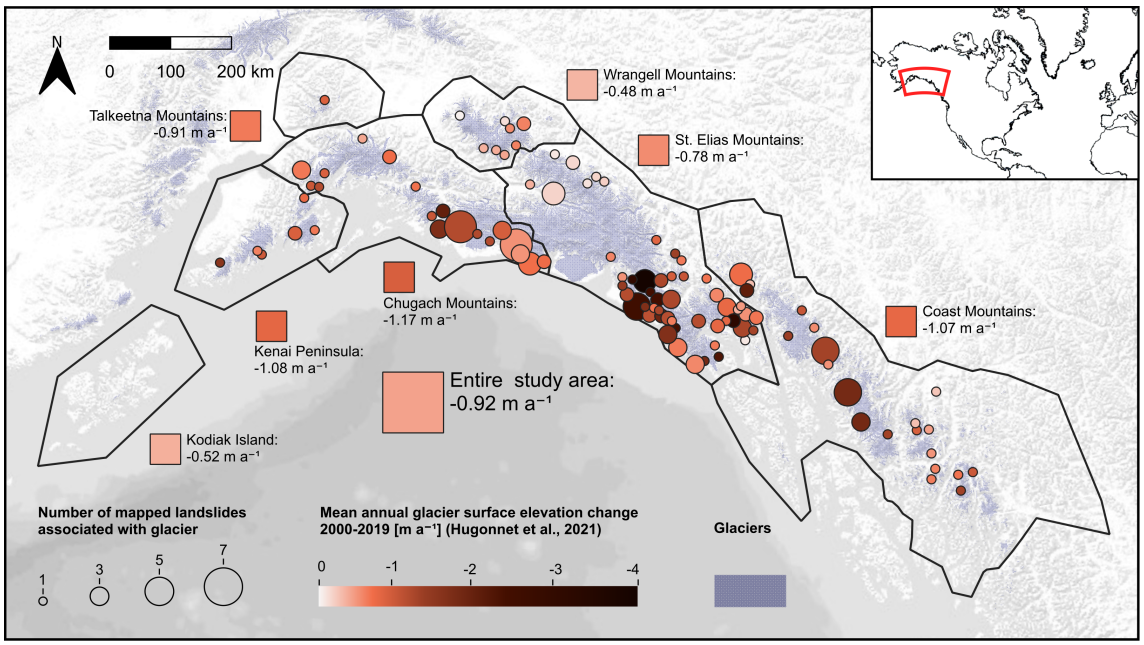

Figure 12: Distribution of mapped landslides in relation to surface elevation change of associated glaciers between 2000 and 2019, based on data from Hugonnet et al. (2021). The number of landslides associated with specific glaciers is presented alongside the mean annual glacier surface elevation change for the respective glacier. For comparison, the mean annual glacier surface elevation change for each region and the entire study area is included. Basemap imagery: ESRI World Terrain.

Overall, 122 of the 182 mapped landslides (67.0 %) are associated with glaciers that have elevation change rates more negative than the area-weighted average of the entire study area (see Fig. 12). 1 landslide could not be associated to any one glacier with reasonable confidence. Region-specific observations include the following are outlined in Table 5.

All mapped landslides are associated with glaciers showing negative elevation changes. 68 mapped landslides are associated with glaciers exhibiting elevation change rates between 0 and -1 m a^{-1}. The majority of mapped landslides (n = 94), are associated with glaciers with elevation change rates between -1 and -2 m a^{-1}. Additionally, 13 landslides are associated with glaciers exhibiting elevation change rates between -2 and -3 m a^{-1}, and 6 landslides are associated to two distinct glaciers with rates between -3 and -4 m a^{-1}. Notably, 4 mapped landslides are associated with the East Yakutat Glacier in the St. Elias Mountains, one of the most rapidly retreating glaciers globally (Trüssel et al., 2013), with a surface elevation change rate of -3.97 m a^{-1} between 2000 and 2019.

Region	N landslides	N below regional average	Percentage
Chugach Mountains	41	18	43.9
Coast Mountains	37	23	62.1
Kenai Peninsula	7	4	57.1
St. Elias Mountains	86	69	80.2
Talkeetna Mountains	1	1	100
Wrangell Mountains	9	7	77.7

Table 5: Fraction of landslides associated with glaciers with surface elevation change below their respective regional average. The non-associated landslide in the Talkeetna Mountains is excluded.

6.3.2. Landslide occurrence in relation to precipitation

Figure 13 shows the distribution of modeled 1981-2010 average annual precipitation for the PRISM grid cells that intersect with mapped landslides, compared to grid cells within the study area and those within a distance equal to the 90th percentile of the distance from mapped landslides to glaciers that do not intersect with mapped landslides. Although the range is much wider for grid cells without mapped landslides, the distributions are shifted. The quantiles of precipitation (25th: 1700.1 mm a^{-1}, 75th: 4220.4 mm a^{-1}) and the median (4220.4 mm a^{-1}) for grid cells intersecting with mapped landslides are higher than those for grid cells without mapped landslides (25th: 1369.8 mm a^{-1}, 75th: 3399.5 mm a^{-1}, median: 2323.9 mm a^{-1}). This suggests that precipitation at detected landslide sites is generally higher compared to slopes at similar distances from glaciers within the study area, where no landslides were detected.

The univariate logistic regression model, using only precipitation as a predictor, revealed a statistically significant positive relationship between the modelled precipitation of a grid cell and the likelihood of a mapped landslide being at least partly within that cell(β_0 = -5.18, β_1 = 0.0002, p-value $<$ 0.0001). For each additional mm of modelled annual precipitation, the log-odds of a mapped landslide occurring increase by 0.0002, which is a considerable effect given the range of mean annual precipitation within the study area (compare to Fig. 13).

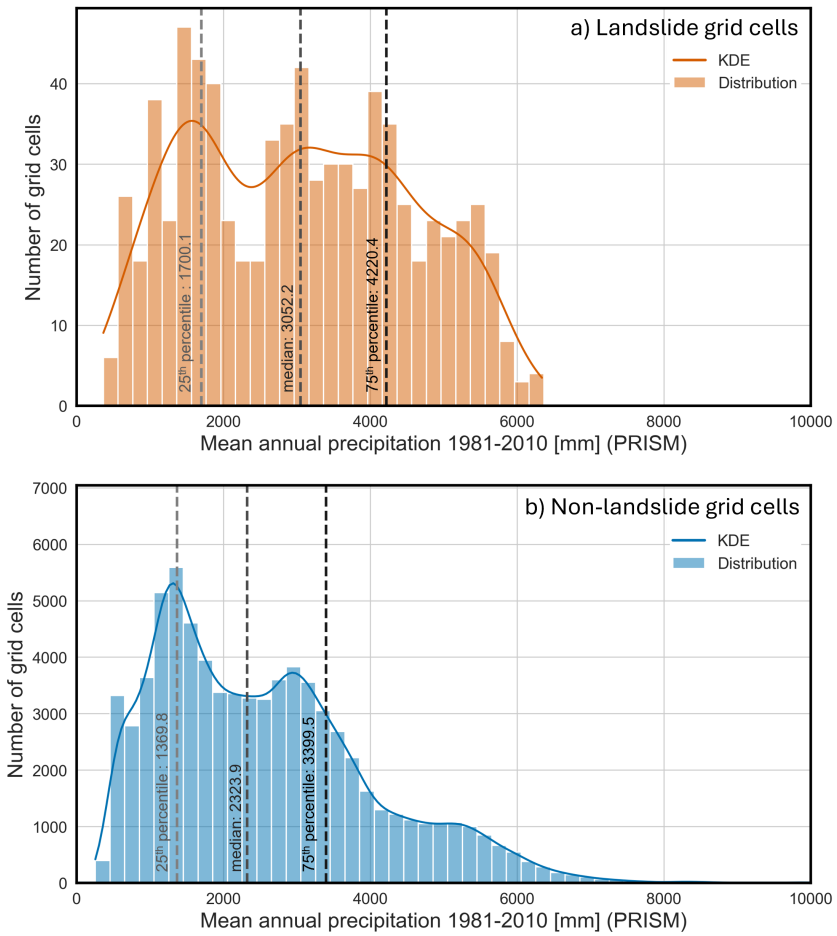

Figure 13: 1981-2010 average annual precipitation in PRISM climate data grid cells, intersecting with mapped landslide compared to sites at comparable distances to glaciers where no landslides were detected.

6.3.3. Mean annual ground temperature and permafrost probability at the landslide sites

Of the 182 mapped landslides, coverage of the mean annual ground temperature dataset was available for 151 landslides. The remaining landslides were located in areas excluded from the dataset due to glacier masking, which partly extends to non-glaciated areas due to the datasets coarse spatial resolution (1 km). The modeled MAGT at the landslide sites range from -3.4 to 4.7 °C and MAGT is below 0 °C or lower for only 13 of these 151 landslides (see Fig. 14). When accounting for one standard deviation of uncertainty, 21 landslide sites have a MAGT below 0 °C when the uncertainty is considered in the negative direction, while only 7 landslides fall below 0 °C when the uncertainty is considered in the positive direction. All landslide sites with negative modeled MAGT are located in the Talkeetna, Wrangell, and northwestern St. Elias Mountains, while MAGT at the landslide sites is higher in the coastal regions.

The permafrost probability, defined as the fraction of model ensemble runs with a MAGT of 0 °C or lower, is 0 for 90 of the 151 considered landslides and below 0.005 for an

additional 20 landslides. This results in a total of 110 landslides being categorized as being in non-permafrost areas. For 16 other landslide sites, the permafrost probability ranges between 0.005 and 0.1, suggesting the presence of isolated permafrost patches. For nine landslide sites, the permafrost probability is between 0.1 and 0.5, indicating sporadic permafrost. Discontinuous permafrost, with occurrence probabilities between 0.5 and 0.9, was found for 7 landslide sites, while 4 sites showed a permafrost probability of over 0.9, indicating continuous permafrost (see Fig. 15).

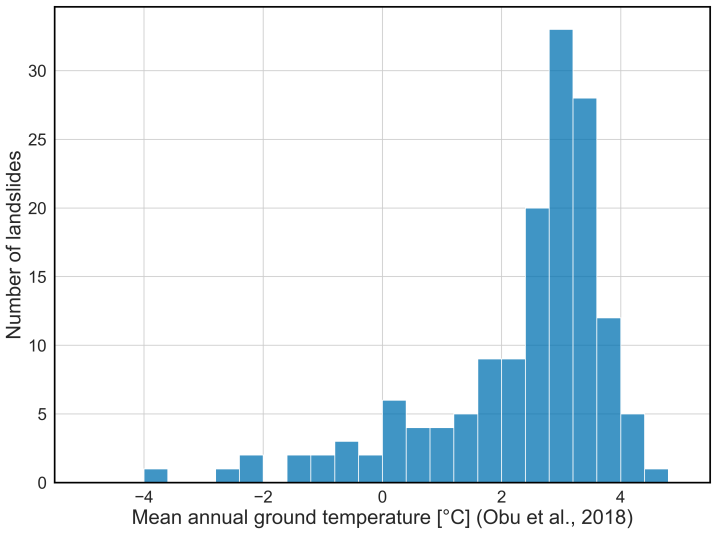

Figure 14: Mean annual ground temperature at the sites of the mapped landslides.

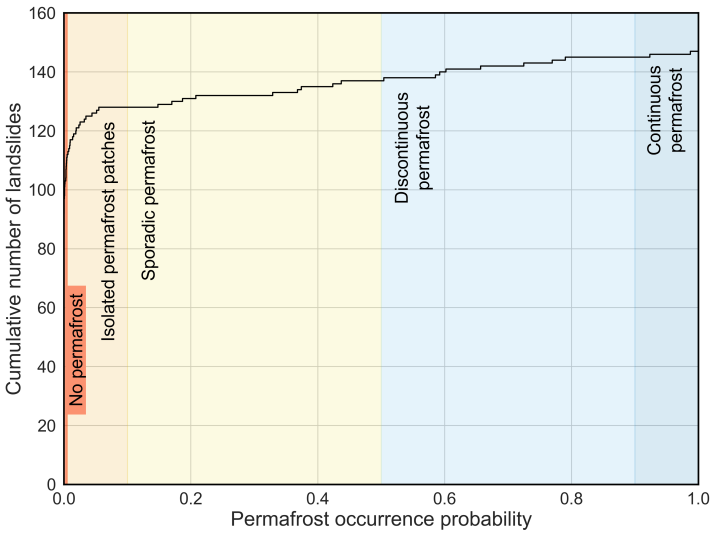

Figure 15: Cumulative number of landslides by permafrost occurrence probability. Shading indicates the permafrost zonation.

6.3.4. Lithological characterization of the landslide sites

Of the 182 mapped landslides, the majority, 120 landslides involve bedrock, 62 occur in surficial deposits. Landslides occurring in bedrock are most frequent in siliclastic sediments, which account for 43 landslides. Within these siliclastic sediments, notable occurrences include volcanic sediments from the Chugach Accretionary Complex (9 landslides), as well as various marine deposits, including Chugach Flysch (8 landslides), the Redwood and Poul Creek formations (7 landslides) marine deposits of the Orca Group (6 landslides) and Yakataga and Tugidak formations (4 landslides), along with turbidite deposits (4 landslides). In addition to siliclastic sediments, mapped landslides are also common in intrusive igneous rock units, with 28 landslides, particularly in granodiorites of the Coast Plutonic Complex (10 landslides) and foliated granitic rocks (5 landslides). 15 landslides were attributed to different units of metamorphic rock. Smaller numbers of landslides were attributed to other lithologies, including igneous extrusive rocks (11 landslides) and tectonic mélanges (9 landslides). A minority of 5 landslides occurred in chemical sediments, and another 5 landslides were attributed to units of the Yakutat Group that could not be assigned to any of the aforementioned categories due to their mixed lithology. Lastly, for 4 landslides, the lithology remains unknown based on the utilized geological maps.

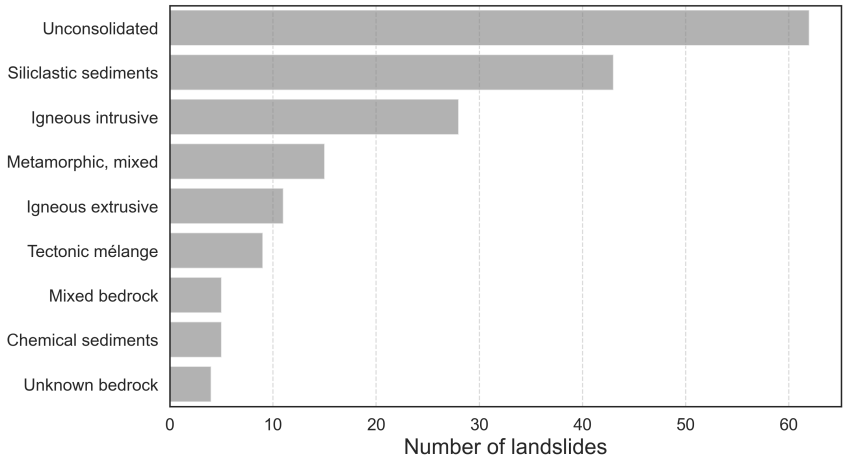

Figure 16: Overview of the lithological setting of the mapped landslides.

7. Discussion

7.1. Effectiveness of ITS_LIVE for manual landslide detection

The first research question investigates the effectiveness and limitations of ITS_LIVE surface velocities for detection of paraglacial landslides over large areas. To answer this, the dataset was used to identify and manually map landslides across southern coastal Alaska, with the results being verified using auxiliary data. A total of 182 landslides were identified and mapped, all of which were confirmed recently have been active with moderate to high certainty, demonstrating a general effectiveness of ITS_LIVE surface velocities for landslide detection.

7.1.1. Limitations of ITS_LIVE for manual landslide detection

In the initial mapping using only ITS_LIVE data, 1677 slope sites were identified to show relatively high velocity compared to their surrounding. However, verification with multi-spectral satellite imagery and hill shades confirmed geomorphological features indicative of instability at only 462 sites. After further verification, only 182 locations were ultimately mapped, confirmed through satellite imagery time series, radar coherence or clear ITS_LIVE signal in combination with clear geomorphic features. The high number of detections without clear instability signs suggests considerable dataset noise. Some may be landslides, but the lack of distinct features indicates a high false positive rate relying on ITS_LIVE data only.

Velocity estimates in the ITS_LIVE data should be considered as uncertain in general. As discussed by Walden et al. (2024), the dataset was designed for the quantification of glacier surface velocities, which are typically much higher than the velocities associated with landslides. The velocity error estimates are not quantitatively reliable, especially for stable or nearly stable surfaces, because they include a correction component based on the method used for velocity bias correction. This correction component ranges from 5 to 100 m a^{-1} (Gardner, Fahnstock, Greene, et al., 2024), rendering it useless for the quantification of uncertainty over stable surfaces. Thus, a velocity threshold above which ground movement can be distinguished from noise can not be defined clearly. In addition, the velocity direction was found to be unreliable in some cases. For 25 out of 182 mapped landslides, the velocity directions did not align with the slope of the terrain. This suggests that while the ITS_LIVE surface velocities reflect general terrain changes, they do not consistently capture the direction or rate of these changes.

The extent to which detection using ITS_LIVE surface velocities may be biased toward certain types of landslides has not been assessed. However, since a feature tracking algorithm is used to derive the velocities, the detection relies on identifying the same features in imagery from repeat satellite passes. For landslides that occur at very high velocities (e.g., falling processes), detection using ITS_LIVE surface velocities may be severely limited.

Another challenge is the coarse 120 m resolution of the dataset, limiting detection to landslides over tens of thousands of square meters. The smallest landslides detected were

represented by no more than 4 pixels, limiting detection of landslides smaller than a few 10'000 square-meters. No landslides smaller than 50'000 m^2 were mapped, and those were less clearly distinguishable from noise than larger instances. Another issue is mixed pixels near glacier margins. Also observed by Walden et al. (2024) this likely results from signal blending through large window sizes used in feature tracking and change of the glacier margin over the observation period. It restricts detection of instabilities within a few pixels (hundreds of meters) beyond glacier margins.

Analysis of topography reveals that landslides mostly occur on south-facing slopes, with some on west and east-facing slopes, and none on north-facing slopes. Some physical factors may help explain these findings, such as large-scale structural geology (e.g., Brideau et al., 2009). However, given the large geologically diverse study area, such an influence of this consistency is unlikely. Increased infiltration through rapid snowmelt on south facing aspects or a connection to permafrost are other possible physical explanations, but they hardly fully explain the encountered aspect distribution, suggesting a dependence of data quality on terrain aspect. This may result from topographic shading in passive Sentinel-2 and Landsat 4, 5, 7, 8 and 9 imagery used for product generation. While Sentinel-2 data is processed at L1C processing level (top-of-the-atmosphere), indicating the potential influence of shadows, processing level of the Landsat data used is unspecified (Gardner, Fahnstock, Greene, et al., 2024). Shading is also a challenge briefly noted by Lei et al. (2021) in describing the feature tracking algorithm used for ITS_LIVE. Additionally, Sentinel-1 acquisition geometry may further influence aspect-dependent data quality, as Gardner, Fahnstock, Greene, et al. (2024) do not specify which geocoding operations were applied to the SAR input data. Apart from input data quality issues, longer snow cover on north-facing slopes may limit image pairs in snow-free conditions that capture terrain changes, reducing the data quality of the ITS_LIVE surface velocities.

7.1.2. Comparison with landslide inventories in the Prince William Sound region

To further assess the strengths and weaknesses of the ITS_LIVE surface velocity dataset for landslide detection, a comparison with two different landslide inventories for the Prince William Sound in southcentral Alaska is made. The comparison may have been limited because these inventories do not solely focus on landslides likely influenced by glaciation. However, this is not considered relevant, as no ITS_LIVE-detected landslides in the area were dismissed for lacking evidence of paraglacial conditioning. In other words, all landslides within these inventories that were detected using ITS_LIVE were included in the preliminary detections or the final inventory.

Higman et al. (2023) compiled an inventory of slope instabilities, integrating information from field observations, optical satellite and aerial imagery, InSAR, and LiDAR surveys. It provides confidence estimates for movement gained from remote sensing sources as well as geomorphological evidence.

Schaefer et al. (2024) used MTInSAR data from 2016 to 2022 to identify landslides in an area similar to the one of Higman et al. (2023), to assess potential for tsunamigenic landslides. Their detection focused on landslide areas larger than 50,000 m^2. Preliminary

detections were confirmed by identifying landslide-typical geomorphological features in high-resolution multispectral imagery and DEMs.

A comparison with the inventory of Higman et al. (2023) reveals that 8 of the 62 landslides mapped in their study are also mapped in this study. An additional 12 landslides identified by Higman et al. (2023) were preliminarily detected in this study, but were not fully mapped due to a lack of movement confirmation. The remaining 42 landslides in the Higman et al. (2023) inventory were not detected in this study. For the landslides mapped in this study, the evidence of active deformation was classified as clear in 4 cases, suggestive in 2 cases, and uncertain and absent in 1 case each by Higman et al. (2023). For the landslides that were preliminarily detected but not mapped, clear evidence of movement was identified in 3 cases, suggestive evidence in 1 case, uncertain evidence in 7 cases and no evidence in 1 case. Of the 42 landslides present in the Higman et al. (2023) inventory but not detected in this study, only 4 exhibit clear signs of active deformation, while 7 show suggestive signs, 23 show uncertain signs and 8 show no signs of deformation. No landslides were mapped in this region that were not also included in the Higman et al. (2023) inventory. However, 6 preliminary detections in this study do not have corresponding equivalents in their dataset. Of these, one is confirmed by the study of Schaefer et al. (2024).

The large number of undetected landslides highlights limitations of detection using ITS_LIVE compared to a combination of multiple sources. Though, some missed landslides may also result from human error and bias. Additionally, 8 undetected landslides were smaller than the smallest detected one (50'520 m^2), indicating size may have contributed to their omission. The fact that 7 out of 11 landslides with clear signs of active deformation from that inventory were detected, suggests ITS_LIVE is better suited for identifying landslides beyond a certain threshold of activity.

Schaefer et al. (2024) identified 43 active landslides in a similar study area. Of these, 7 were detected and mapped in this study, while an additional 11 were preliminarily detected but not ultimately mapped. Since their study used MTInSAR between 2016 and 2022, which overlaps with the ITS_LIVE data from 2014 to 2022, it suggests that all of these landslides exhibited some activity during this period. Thus, detection using MTinSAR is clearly more sensitive than using ITS_LIVE composites. However, in this study, 7 landslides were detected and mapped that were not identified in Schaefer et al. (2024), and 39 preliminary detections from this study are not included in their inventory. This proposes that ITS_LIVE could complement other detection methods.

7.1.3. Future perspectives

Given its global coverage of glaciated regions, ITS_LIVE surface velocity products can be used to detect landslides in other glaciated areas, while considering the limitations discussed. Hence, the dataset could serve as an accessible complementary resource for landslide detection worldwide, and in that way contribute to understanding of paraglacial processes and hazard mitigation efforts. To better understand its usability, future research should focus on evaluating the reliability of the velocity estimates by testing them against well-monitored landslides, and also address aspect-dependent data quality issues.

7.2. Landslide detection using a convolutional neural network

The second research question focuses on the effectivity of a convolutional neural network trained on the mapped landslides, ITS_LIVE surface velocities and auxilliary data in detecting landslides. This was assessed by training a Mask-R-CNN model using different input data cases. From the insights gained from the training and testing of the model, suggestions for further improvement are made.

7.2.1. Implications of training performance

The loss functions provide valuable insights into model performance across epochs. The training loss exhibited an exponential decrease across all cases, indicating successful learning. This trend is expected as the model converges, with the exponential decay of the learning rate also contributing to stabilization in later epochs. However, training loss was noticeably higher for Case VII, where data augmentation increased input tiles by a factor of four, making it harder for the model to represent all tiles with a good fit. After initial epochs, all components except the mask head showed low losses in Cases I to VI, suggesting strong fit to the training data. The higher mask loss is assumed to partly stem from ambiguity in manual landslide delineation, limiting the clarity of the ground truth masks. In case VII, also the RPN region proposal and head bounding box losses were a clear contributor, which shows that the representation of the training data within these components of the model is meaningfully less optimal with an increased amount of input data.

For all cases, validation loss remained clearly higher than training loss. This indicates poor generalization. While it initially decreased (except in Case VI), it later increased after 20–40 epochs, except in Case VII. This signals overfitting, as in the same epochs training loss is still increasing, but these improvements do not translate to the validation data. Mask and bounding box losses from the model head contributed more in validation than in training, not only for Case VII but also for cases I–VI. This confirms that their lower contribution in the training for cases I–VI is due to overfitting.

The most important factor of rising validation loss was increased RPN region proposal loss. Hence, the model struggles most with generating region proposals rather than refining the existing proposals. This could stem from a lack of relevant information in the input channels or insufficient annotations (landslide masks and bounding boxes), with the latter explaining why augmentation improved this issue. The omission of the RGI inventory notably increased this loss component, suggesting that explicit glacier representation helps in the generation of region proposals, possibly either by excluding glacier-covered areas or by establishing a relationship of landslide proximity to glaciers.

7.2.2. Model sensitivity to input data cases

Performance was poorest when all input channels were included, and performance improvements were observed with the omission of any channel. This is in contradiction with the assumption that more data automatically leads to better performance. It has been

discussed widely that with increasing number of dimensions, the need for data in machine learning algorithms rises exponentially (e.g., Altman & Krzywinski, 2018). CNNs mitigate this through strategies like dimensionality reduction in pooling layers (Abend, 2022), still, the issue persists. Similar findings were made by Sameen and Pradhan (2019), who used multispectral imagery for landslide detection using different CNNs. They also conducted sensitivity analysis by incorporating DEMs and DEM derivatives but observed that these inclusions reduced performance.

Omitting only the velocity directions improved performance compared to excluding both velocity magnitudes and directions, resulting in the best model performance without data augmentation. This suggests two main takeaways: first, velocity direction information in its current form is not beneficial to the model. No previous studies were found that used azimuthal information in CNNs, either as Cartesian coordinates or otherwise. Hence, it remains unclear whether this lack of value is due to overfitting, noise in the directional components (discussed in Section 7.1.1), the model's inability to extract meaningful information from the directions split into two channels, or relate them to information in other input channels. However, assuming that adding more channels worsens overfitting, the fact that the model performs better with velocity magnitudes included than with all velocity channels excluded, strongly indicates that inclusion of ITS_LIVE velocity magnitudes is beneficial for detection performance.

However, omission of the DEM and Sentinel data results in worse performance than omission of ITS_LIVE data. These datasets were included as they were crucial for confirmation of landslides in manual mapping. Bad performance with their exclusion demonstrates this role. The poor bounding box alignment when Sentinel data is excluded highlights the importance of this information in accurately detecting the landslide extent, which is expected as this data was the primary source for their delineation in manual mapping, and the extent of landslides as interpreted from other data sources may vary, for instance if parts of it display low velocities due to inactivity. Omitting the DEM, however, results in the best bounding box alignment, suggesting that the information from this channel leads to bounding box positions that conflict with those derived from the other channels.

Omitting the RGI inventory resulted in high precision but low recall and poor bounding box alignment. This proposes that the RGI inventory is useful for detecting landslide locations. It possibly helps to establish a spatial relationship between landslides and glaciers, which other channels do not capture as explicitly. However, it does not appear to prevent false negatives better compared to other input channels, in way similar to how Shi et al. (2021) prevented false positives through the integration of infrastructure data to prevent misclassifications between landslides and anthropogenic structures.

Notably, case VII showed the best balance of precision, recall, and bounding box alignment, also in comparison to its non-augmented counterpart. This demonstrates that improved generalizability is achieved through data augmentation and that the limited input data size is one of the main constraints of the model at this stage.

7.2.3. Final performance evaluation

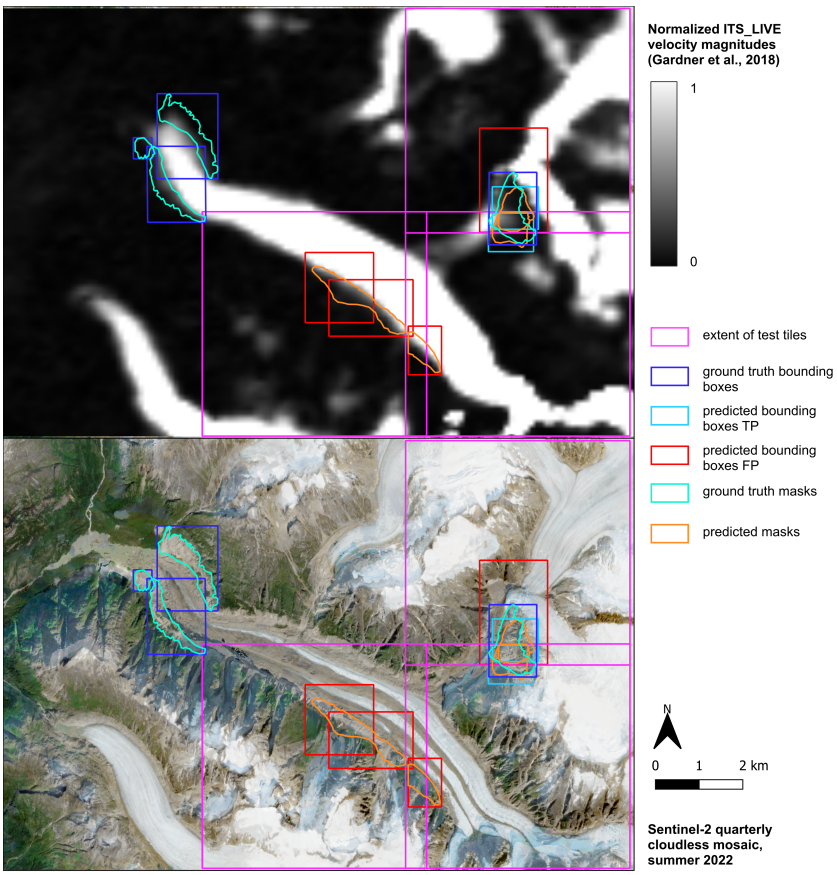

Figure 17: Example of model test detections and mask segmentations generated using the best model weights of input data case VII.

Figure 17 illustrates both the strengths and weaknesses of the current model. The pink boxes indicate the test tile boundaries where predictions were made, while other areas belong to the training or validation data. Dark blue represents the ground truth bounding boxes, and turquoise represents the ground truth masks. The landslide in the eastern part of the image was correctly detected (light blue bounding boxes) independently in both test tiles that it overlaps. In the upper tiles, there was a double prediction (red box), which counts as a false negative. The predicted segmentation masks (orange) generally identify the landslide well, particularly in areas with higher surface velocities (upper panel), where the ground cover largely matches the ground truth mask.

However, in the lower panel, three false positives were detected along with their associated masks. These false positives are similar to both the velocity data (due to pixel mixing at the glacier margin) and surface characteristics to the three landslides near the glacier terminus. This similarity may explain their false detection, even though no actual movement could be confirmed at these locations.

The observed results in this study showed poor precision (0.2) but fair recall (0.53), leading to a fairly poor F1-Score (0.29) and mean IoU (0.34). When comparing these findings

to other studies, several considerations should be taken into account. Firstly, a minimal mean IoU (> 0) threshold was used to define true positives. This choice is justified by the high uncertainty associated with delineating landslide polygons in manual mapping. If a higher threshold were used to define true positives, the performance metrics would be lower. Secondly, this study covers a large area with considerable spatial resolution, making it impractical to process all tiles while maintaining computational efficiency. As a result, tiles without known landslides were included to match the number of tiles containing landslides. However, in a real-world application of the model over larger areas, this approach could lead to an increased number of false positives, if it is employed in areas where landslides are sparse.

For a landslide segmentation study in Malaysia, Sameen and Pradhan (2019) used multi-spectral data, combined partly with DEM and DEM derivatives, and achieved F1 scores ranging from 0.60 to 0.77 and mean IoUs between 0.60 and 0.78 using a training dataset of 152 landslides. In a similar segmentation task using different combinations of SAR imagery, DEMs and DEM derivatives, (Nava et al., 2022) achieved F1 scores between 0.50 and 0.61, with mean IoUs ranging from 0.34 to 0.44. This was based on a dataset of 941 landslide tiles, with 80 % used for training.

For tasks focusing solely on detection, Cai et al. (2023) achieved F1 scores of 0.91 in landslide detection using DEM data and interferograms, based on 516 training samples. Similarly, Qin et al. (2023) reported F1 scores of 0.8 for bounding box predictions using only spectral imagery, using 554 training samples but relying on extensive data augmentation.

However, with exception of Sameen and Pradhan (2019) the number of training samples used in the above-mentioned studies exceeds those used here (80 % of 182 landslides) by a large margin. This supports the proposition that poor performance is in part due to a lack of sufficient training data, but that high performance could also be achieved with input data that is low in noise and optimized model structures.

Yet, the studies mentioned for comparison are typically focused on much smaller, more homogeneous study areas, where a high density of landslides is observed. In the case of Nava et al. (2022), for instance, the landslides are assumed to have been triggered by the same earthquake. Hence, these landslides share similar appearance due to common geology, land cover, and similar landslide process types. It also appears that many studies, including those by Nava et al. (2022), Qin et al. (2023), and Sameen and Pradhan (2019) focus on debris or earth flows, the deposits of which are well distinguishable from background, if recent.

In contrast, this study covers a much larger area, where landslides occur in a wide range of geological and geomorphological settings and span different landslide process types. Additionally, the study area is characterized by highly active terrain, where movement (e.g., glaciers and rock glaciers), surfaces resembling those of landslides (e.g., glacial deposits) and topographic features similar to those of landslides (e.g., fluvial banks) are widespread and may be subject to misclassification. As a result, distinguishing landslides from the surrounding landscape becomes more challenging, not only to human interpreters, but also algorithms trained on their mappings.

7.2.4. Further development

The main challenges facing the model were identified as suboptimal performance of the RPN component and overfitting, which may be caused by either a high number of channels or a low number of training samples. It can be assumed that addressing these issues could lead to a significant improvement in the model's performance that will however still be limited to some degree by noise and uncertainty of manually mapped input data.

A reasonable starting point for further development would be to conduct systematic sensitivity tests focused on hyperparameters related to the RPN component. Key parameters to explore include the RPN anchor scales, aspect ratios, the number of proposed ROIs, and the balance between positive and negative ROIs. Additionally, the classification components of the model (both in the head and RPN) should be investigated more closely, as they reported very low losses, yet misclassifications were abundant in the final results. The potential influences of the class imbalance present in the dataset may be a starting point for this analysis.

To counteract overfitting, one promising approach would be to experiment further with the input channels to find the optimal balance between the minimum number of channels and the amount of valuable information provided. The improved performance with data augmentation suggests that more extensive data augmentation would be beneficial. Geometric and photometric augmentation methods could be explored. Geometric transformations, such as rotations or distortions of the input tiles, could be applied easily, while photometric methods (such as e.g., by Qin et al. (2023)) that alter pixel values should be used more cautiously, as the pixel values of the channels are related to physical properties such as velocity or elevation. Lastly, increasing the number of mapped landslides would be the most straightforward solution to combat overfitting, although also the most time-consuming.

7.3. Connections between landslide occurrence and environmental factors

The third research question examined the relationship between environmental factors involved in the preconditioning, preparation, and triggering of paraglacial slope instabilities and the landslides that were manually detected. The results provide an overview of the relevant patterns, offering insights that can help direct more focused investigations in the future.

7.3.1. Connections between landslide occurrence and glacier mass loss

While glacier mass loss does not need to correspond directly to glacier retreat — such as in the case of surging glaciers — or result in uniform thinning across the entire glacier area, it is still considered a useful proxy for both retreat and thinning.

In its imprecision regarding the structural and spatial relationship between the examined landslides and glaciers and its imprecision regarding temporal evolution, this analysis does not allow conclusive statements about the certainty of paraglacial conditioning or the mechanism at play. Yet, it agrees well with previous findings linking glacier change to

landslide activity. The mapped landslides occurred predominantly associated with above-average mass loss, supporting previous studies that link landslide activity to glacier retreat and thinning (Dai et al., 2022; Lacroix et al., 2022; Walden et al., 2024). This also aligns with the findings of Kos et al. (2016), who reported that landslides can become active when ice loss surpasses a critical threshold. Additionally, it is consistent with research showing that landslide velocity is influenced by the presence or absence of ice at the landslide toe (McColl & Davies, 2013; Storni et al., 2020).

While the results point towards glaciation playing a role in the activity pattern of the detected landslides, their history is unknown. Glaciation and deglaciation are recognized as factors influencing slope stability across multiple glacial cycles (Grämiger et al., 2017, 2018, 2020; McColl, 2012). Therefore, the potential preparatory effects of past glaciation and deglaciation on these slopes may extend far back in time. Assuming some degree of persistence in climatic patterns and their interaction with glacial systems, it is cautiously hypothesized that the glaciers currently experiencing high mass loss may have also undergone significant fluctuations in past glaciations, potentially contributing to repeat amplified preparatory influences at the same sites.

7.3.2. Connections between landslide occurrence and precipitation

On average, precipitation was higher at landslide sites compared to sites at comparable distance to glaciers without mapped landslides. However, this comparison has limitations. The use of glacier proximity as a measure for comparable slopes may lead to the inclusion of areas without potential for landslides, such as low-relief terrain. Thus, while providing useful context, these results should be interpreted cautiously. In spite of these uncertainties, mapped landslides were more frequent in precipitation-rich coastal regions than in the drier interior regions, more qualitatively supporting a link between precipitation and landslides.

The precipitation dataset (1981–2010) predates the landslide velocity observations (2014 – 2022). It is thus more representative of predating preparatory climatic influences than direct triggering influences. However, the latter is still true under the assumption of persistence of the general patterns in precipitation.

It remains unclear from these findings whether long-term precipitation, extreme rainfall events correlated with annual precipitation, or water availability from snowmelt (Huggel et al., 2012; Iverson, 2000; Le Roux et al., 2009) play the most significant role in influencing landslide activity. Additionally, it is uncertain whether precipitation primarily contributes through long-term weathering processes or by triggering landslides via increased pore-water pressure following infiltration. Further investigations that are more specific about temporal patterns in precipitation and landslide activity and are focussed more on single mechanism would be beneficial in better understanding these links.

7.3.3. Relevance of permafrost

The majority of landslides occurred in areas with positive modelled MAGT, indicating low or no permafrost probability. Given the clarity of the result, uncertainties introduced by the uncertainties of the dataset and its coarse spatial resolution do not question the

results, as the absence persists for most sites under consideration of the reported validation accuracy of 2 C of the dataset.

A MAGT close to zero would indicate the possibility for warm or degrading permafrost, which has a destabilizing effect on slopes (Davies et al., 2001; Deline et al., 2021; Krautblatter et al., 2013; Matsuoka & Murton, 2008). While such an influence is unlikely for present conditions following from the results, it may well be the case that permafrost degradation did play a role in previously preparing or triggering the slopes which were detected as active landslides.

7.3.4. Relevance of lithology

The high susceptibility of certain rock units to landslides, as reported in this study, is consistent with findings from other research. Siliciclastic sedimentary rocks, particularly volcaniclastic sediments of the Chugach Accretionary Complex, Chugach flysch, marine deposits, and igneous intrusive rocks are among the most common lithologies that host the detected landslides. A high susceptibility Of Yakutat Flysch and igneous intrusives has been reported by (Bessette-Kirton & Coe, 2020) for rock avalanches in the Saint Elias Mountains. The frequent occurrence of landslides in volcaniclastic sediments may be attributed to their tendency to weather into clay minerals, which reduce rock strength, as noted by Patton et al. (2020) in the Alaska Range. Similarly, different siliclastic marine deposits have been widely documented as landslide-prone due to contrasting permeabilities (e.g., Hansen et al., 2011). These susceptibilities may help explain the clustering of landslides in the southeastern Chugach Mountains and the southeastern St. Elias Mountains, where marine deposits, including Flysch, are prevalent.

Many landslides were also found in unconsolidated rocks, similar to findings for a study of recent landslides by Patton et al. (2020) in the Alaska range. However, landslides in unconsolidated material must be interpreted differently in the context of glacier change compared to those in bedrock. Processes such as glacially induced fracturing and jointing (Fischer et al., 2010; Grämiger et al., 2017, 2018, 2020; Nichols, 1980) which influence landslides in bedrock, cannot be assumed to apply to unconsolidated deposits.

8. Conclusions

A total of 182 active landslides across Southern Alaska were successfully detected and mapped using ITS_LIVE velocity data, highlighting the dataset's potential for landslide detection. However, several limitations were identified, including a high noise-to-signal ratio, which requires confirmation of detections with additional datasets. An unusually high skew in the aspect distribution suggests that data quality issues may hinder landslide detection on northern slopes. Comparison with other inventories indicates that ITS_LIVE is more effective at detecting landslides with pronounced activity. However, the lack of clearly defined uncertainty estimates for the absolute velocity values prevented the establishment of a detectability threshold. Despite these challenges, ITS_LIVE velocities prove valuable as a complementary data source for landslide detection in glaciated regions worldwide, potentially offering insights into paraglacial processes and supporting hazard management efforts.

At this stage, the CNN's detection performance is limited, showing promising recall but poor precision and alignment of prediction bounding boxes. The impact of different auxiliary input channels varies: ITS_LIVE surface velocities, Sentinel-2 multispectral imagery, DEMs, and the RGI inventory each provide valuable information for different aspects of the model, while ITS_LIVE velocity directions do not provide value. However, maximizing the number of input data channels tends to worsen performance, pointing out the need for further experimentation and careful selection of input data channels. When input data was augmented, the model performed better, but overfitting remains a significant issue. This suggests that future improvements should focus on expanding the training data, either by increasing data augmentation or incorporating more landslide mappings. Despite these adjustments, the model's performance may still be constrained by the high noise in ITS_LIVE velocity data and the inherent challenges of detecting landslides in mountainous terrain.

Analysis of the manually mapped landslides reveals preferential occurrence of landslides around glaciers with an above-average negative surface elevation change, supporting previous research linking landslide activation to glacier retreat and thinning. Average annual precipitation levels at the landslide sites are comparatively high, pointing to a potential influence of wet climate on preparing or triggering the detected landslides. Permafrost, does not appear to be a relevant factor at most detected sites, at least in present times. The lithological analysis reveals that many landslides occur in unconsolidated surficial deposits, siliclastic marine deposits, volcaniclastic sediments, and igneous intrusive rocks. This distribution aligns with susceptibility patterns found in the literature and helps explain the spatial distribution of the detected landslides.

9. Data and code availability

The mapped landslide inventory, and model code together with input data and the best performing model weights can be found at https://doi.org/10.5281/zenodo.14768586

References

Abdulla, W. (2017). *Mask R-CNN for object detection and instance segmentation on Keras and TensorFlow*. Retrieved January 7, 2025, from https://github.com/matterport/Mask_RCNN

Abend, K. (2022). How Convolutional Neural Networks Defy the Curse of Dimensionality: Deep Learning Explained. *TechRxiv*. https://doi.org/10.36227/techrxiv.18316439.v1

Allen, S., Cox, S., & Owens, I. (2011). Rock avalanches and other landslides in the central Southern Alps of New Zealand: A regional study considering possible climate change impacts. *Landslides*, *8*, 33–48. https://doi.org/10.1007/s10346-010-0222-z

Altman, N., & Krzywinski, M. (2018). The curse(s) of dimensionality. *Nature Methods*, *15*(6), 399–400. https://doi.org/10.1038/s41592-018-0019-x

Augustinus, P. (1995). Rock mass strength and the stability of some glacial valley slopes. *Zeitschrift für Geomorphologie*, 55–68. https://doi.org/10.1127/zfg/39/1995/55

Ballantyne, C. K. (2002). Paraglacial geomorphology. *Quaternary Science Reviews*, *21*(18), 1935–2017. https://doi.org/10.1016/S0277-3791(02)00005-7‘

Bekryaev, R. V., Polyakov, I. V., & Alexeev, V. A. (2010). Role of Polar Amplification in Long-Term Surface Air Temperature Variations and Modern Arctic Warming [Section: Journal of Climate]. https://doi.org/10.1175/2010JCLI3297.1

Bell, D. H. (1976). Slope evolution and slope stability, Kawarau valley, Central Otago, New Zealand. *Bulletin of the International Association of Engineering Geology - Bulletin de l'Association Internationale de Géologie de l'Ingénieur*, *13*(1), 5–16. https://doi.org/10.1007/BF02634752

Bessette-Kirton, E. K., & Coe, J. A. (2020). A 36-Year Record of Rock Avalanches in the Saint Elias Mountains of Alaska, With Implications for Future Hazards. *Frontiers in Earth Science*, *8*. https://doi.org/10.3389/feart.2020.00293

Bovis, M. J. (1982). Uphill-facing (antislope) scarps in the Coast Mountains, southwest British Columbia. *GSA Bulletin*, *93*(8), 804–812. https://doi.org/10.1130/0016-7606(1982)93<804:UASITC>2.0.CO;2

Brideau, M.-A., Yan, M., & Stead, D. (2009). The role of tectonic damage and brittle rock fracture in the development of large rock slope failures. *Geomorphology*, *103*(1), 30–49. https://doi.org/10.1016/j.geomorph.2008.04.010

Brown, J., Ferrians Jr, O. J., Heginbottom, J. A., & Melnikov, E. S. (1997). *Circum-Arctic map of permafrost and ground-ice conditions* (Circum-Pacific Map No. 45). https://doi.org/10.3133/cp45

Brueseke, M. E., Benowitz, J. A., Trop, J. M., Davis, K. N., Berkelhammer, S. E., Layer, P. W., & Morter, B. K. (2019). The Alaska Wrangell Arc: 30 Ma of subduction-related magmatism along a still active arc-transform junction. *Terra Nova*, *31*(1), 59–66. https://doi.org/10.1111/ter.12369

Burrows, K., Walters, R. J., Milledge, D., & Densmore, A. L. (2020). A systematic exploration of satellite radar coherence methods for rapid landslide detection. *Natural Hazards and Earth System Sciences*, *20*(11), 3197–3214. https://doi.org/10.5194/nhess-20-3197-2020

Burrows, K., Walters, R. J., Milledge, D., Spaans, K., & Densmore, A. L. (2019). A New Method for Large-Scale Landslide Classification from Satellite Radar. *Remote Sensing*, *11*(3), 237. https://doi.org/10.3390/rs11030237

Cai, J., Zhang, L., Dong, J., Guo, J., Wang, Y., & Liao, M. (2023). Automatic identification of active landslides over wide areas from time-series InSAR measurements using Faster RCNN. *International Journal of Applied Earth Observation and Geoinformation*, *124*, 103516. https://doi.org/10.1016/j.jag.2023.103516

Caine, N. (1982). Toppling failures from alpine cliffs on ben Lomond, Tasmania. *Earth Surface Processes and Landforms*, *7*(2), 133–152. https://doi.org/10.1002/esp.3290070207

Calkin, P. E. (1988). Holocene glaciation of Alaska (and Adjoining YUKON Territory, Canada). *Quaternary Science Reviews*, *7*(2), 159–184. https://doi.org/10.1016/0277-3791(88)90004-2

Calkin, P. E., Wiles, G. C., & Barclay, D. J. (2001). Holocene coastal glaciation of Alaska. *Quaternary Science Reviews*, *20*(1), 449–461. https://doi.org/10.1016/S0277-3791(00)00105-0

Casagli, N., Intrieri, E., Tofani, V., Gigli, G., & Raspini, F. (2023). Landslide detection, monitoring and prediction with remote-sensing techniques [Publisher: Nature Publishing Group]. *Nature Reviews Earth & Environment*, *4*(1), 51–64. https://doi.org/10.1038/s43017-022-00373-x

Church, M., & Ryder, J. M. (1972). Paraglacial Sedimentation: A Consideration of Fluvial Processes Conditioned by Glaciation. *GSA Bulletin*, *83*(10), 3059–3072. https://doi.org/10.1130/0016-7606(1972)83[3059:PSACOF]2.0.CO;2

Cossart, E., Braucher, R., Fort, M., Bourlès, D. L., & Carcaillet, J. (2008). Slope instability in relation to glacial debuttressing in alpine areas (Upper Durance catchment, southeastern France): Evidence from field data and 10Be cosmic ray exposure ages. *Geomorphology*, *95*(1), 3–26. https://doi.org/10.1016/j.geomorph.2006.12.022

Crosetto, M., Monserrat, O., Cuevas-González, M., Devanthéry, N., & Crippa, B. (2016). Persistent Scatterer Interferometry: A review. *ISPRS Journal of Photogrammetry and Remote Sensing*, *115*, 78–89. https://doi.org/10.1016/j.isprsjprs.2015.10.011

Cruden, D. M. (1991). A simple definition of a landslide. *Bulletin of the International Association of Engineering Geology*, *43*(1), 27–29. https://doi.org/10.1007/BF02590167

Cruden, D. M., & Varnes, D. J. (1996). Landslide Types and Processes. *Transportation Research Board, U.S. National Academy of Sciences, Special Report*, *247*, 36–75. Retrieved January 2, 2025, from https://www.researchgate.net/publication/269710331_CrudenDMVarnes_DJ1996_Landslide_Types_and_Processes_Transportation_Research_Board_US_National_Academy_of_Sciences_Special_Report_247_36-75

Dai, B., Zhang, Y., Ding, H., Xu, Y., & Liu, Z. (2022). Characteristics and Prediction of the Thermal Diffusivity of Sandy Soil. *Energies*, *15*, 1524. https://doi.org/10.3390/en15041524

Dai, C., Higman, B., Lynett, P. J., Jacquemart, M., Howat, I. M., Liljedahl, A. K., Dufresne, A., Freymueller, J. T., Geertsema, M., Ward Jones, M., & Haeussler, P. J. (2020). Detection and Assessment of a Large and Potentially Tsunamigenic Periglacial

Landslide in Barry Arm, Alaska. *Geophysical Research Letters*, *47*(22). https://doi.org/10.1029/2020GL089800

Daly, C., Smith, J., & Halbleib, M. (2018). 1981-2010 High-Resolution Temperature and Precipitation Maps for Alaska. https://prism.oregonstate.edu/projects/alaska.php

Davies, M. C. R., Hamza, O., & Harris, C. (2001). The effect of rise in mean annual temperature on the stability of rock slopes containing ice-filled discontinuities. *Permafrost and Periglacial Processes*, *12*(1), 137–144. https://doi.org/10.1002/ppp.378

Deline, P., Gruber, S., Amann, F., Bodin, X., Delaloye, R., Failletaz, J., Fischer, L., Geertsema, M., Giardino, M., Hasler, A., Kirkbride, M., Krautblatter, M., Magnin, F., McColl, S., Ravanel, L., Schoeneich, P., & Weber, S. (2021). Ice loss from glaciers and permafrost and related slope instability in high-mountain regions. In W. Haeberli & C. Whiteman (Eds.), *Snow and Ice-Related Hazards, Risks, and Disasters (Second Edition)* (pp. 501–540). Elsevier.

ESA. (2024). Sentinel-2 Quarterly Cloudless Mosaic. Retrieved January 1, 2025, from https://dataspace.copernicus.eu/news/2024-2-27-exploring-new-frontier-sentinel-cloudless-mosaics-copernicus-data-space-ecosystem

Esri, Maxar, Earthstar Geographics, & GIS User Community. (2024). World Imagery. Retrieved January 1, 2025, from https://services.arcgisonline.com/ArcGIS/rest/services/World_Imagery/MapServer

Eyles, N., & Kocsis, S. P. (1989). Reply to M. Church and J.M. Ryder's discussion of "sedimentology and clast fabrics of subaerial debris flow facies in glacially-influenced alluvial fan". *Sedimentary Geology*, *65*(1), 197–198. https://doi.org/10.1016/0037-0738(89)90017-1

Fan, X., Dufresne, A., Siva Subramanian, S., Strom, A., Hermanns, R., Tacconi Stefanelli, C., Hewitt, K., Yunus, A. P., Dunning, S., Capra, L., Geertsema, M., Miller, B., Casagli, N., Jansen, J. D., & Xu, Q. (2020). The formation and impact of landslide dams – State of the art. *Earth-Science Reviews*, *203*, 103116. https://doi.org/10.1016/j.earscirev.2020.103116

Fang, C., Fan, X., Zhong, H., Lombardo, L., Tanyas, H., & Wang, X. (2022). A Novel Historical Landslide Detection Approach Based on LiDAR and Lightweight Attention U-Net. *Remote Sensing*, *14*(17), 4357. https://doi.org/10.3390/rs14174357

Fischer, L., Kääb, A., Huggel, C., & Noetzli, J. (2006). Geology, glacier retreat and permafrost degradation as controlling factors of slope instabilities in a high-mountain rock wall: the Monte Rosa east face. *Natural Hazards and Earth System Sciences*, *6*(5), 761–772. https://doi.org/10.5194/nhess-6-761-2006

Fischer, L., Amann, F., Moore, J. R., & Huggel, C. (2010). Assessment of periglacial slope stability for the 1988 Tschierva rock avalanche (Piz Morteratsch, Switzerland). *Engineering Geology*, *116*(1), 32–43. https://doi.org/10.1016/j.enggeo.2010.07.005

French, H. M. (2007). Introduction. In *The Periglacial Environment* (pp. 1–15). John Wiley & Sons, Ltd. Retrieved January 1, 2025, from https://onlinelibrary.wiley.com/doi/abs/10.1002/9781118684931.ch1

Fu, R., He, J., Liu, G., Li, W., Mao, J., He, M., & Lin, Y. (2022). Fast Seismic Landslide Detection Based on Improved Mask R-CNN. *Remote Sensing*, *14*(16), 3928. https://doi.org/10.3390/rs14163928

Gabriel, A. K., Goldstein, R. M., & Zebker, H. A. (1989). Mapping small elevation changes over large areas: Differential radar interferometry. *Journal of Geophysical Research: Solid Earth*, *94*, 9183–9191. https://doi.org/10.1029/JB094iB07p09183

Gardner, A. S., Fahnstock, M. A., Greene, C. A., Kennedy, J. H., Scambos, T. A., & Liukis, M. (2024). DRAFT, Documentation ITS_LIVE Regional Glacier and Ice Sheet Surface Velocities Version 2 [not public].

Gardner, A. S., Fahnstock, M. A., & Scambos, T. A. (2024). ITS_LIVE Regional Glacier and Ice Sheet Surface Velocities: Version 2, data archived at National Snow and Ice Data Center. https://doi.org/10.5067/6II6VW8LLWJ7

Gardner, A. S., Moholdt, G., Scambos, T., Fahnstock, M., Ligtenberg, S., van den Broeke, M., & Nilsson, J. (2018). Increased West Antarctic and unchanged East Antarctic ice discharge over the last 7 years. *The Cryosphere*, *12*(2), 521–547. https://doi.org/10.5194/tc-12-521-2018

Ghorbanzadeh, O., Blaschke, T., Gholamnia, K., Meena, S. R., Tiede, D., & Aryal, J. (2019). Evaluation of Different Machine Learning Methods and Deep-Learning Convolutional Neural Networks for Landslide Detection. *Remote Sensing*, *11*(2), 196. https://doi.org/10.3390/rs11020196

Gill, J. C., & Malamud, B. D. (2014). Reviewing and visualizing the interactions of natural hazards. *Reviews of Geophysics*, *52*(4), 680–722. https://doi.org/10.1002/2013RG000445

Glade, T., & Crozier, M. J. (2005). The Nature of Landslide Hazard Impact. In *Landslide Hazard and Risk* (pp. 41–74). John Wiley & Sons, Ltd. Retrieved August 14, 2024, from https://onlinelibrary.wiley.com/doi/abs/10.1002/9780470012659.ch2

Glueer, F., Loew, S., & Manconi, A. (2020). Paraglacial history and structure of the Moosfluh Landslide (1850–2016), Switzerland. *Geomorphology*, *355*, 106677. https://doi.org/10.1016/j.geomorph.2019.02.021

Grämiger, L. M., Moore, J. R., Gischig, V. S., Ivy-Ochs, S., & Loew, S. (2017). Beyond debuttressing: Mechanics of paraglacial rock slope damage during repeat glacial cycles. *Journal of Geophysical Research: Earth Surface*, *122*(4), 1004–1036. https://doi.org/10.1002/2016JF003967

Grämiger, L. M., Moore, J. R., Gischig, V. S., & Loew, S. (2018). Thermomechanical Stresses Drive Damage of Alpine Valley Rock Walls During Repeat Glacial Cycles. *Journal of Geophysical Research: Earth Surface*, *123*(10), 2620–2646. https://doi.org/10.1029/2018JF004626

Grämiger, L. M., Moore, J. R., Gischig, V. S., Loew, S., Funk, M., & Limpach, P. (2020). Hydromechanical Rock Slope Damage During Late Pleistocene and Holocene Glacial Cycles in an Alpine Valley. *Journal of Geophysical Research: Earth Surface*, *125*(8), e2019JF005494. https://doi.org/10.1029/2019JF005494

Haeussler, P. J., Gulick, S. P. S., McCall, N., Walton, M., Reece, R., Larsen, C., Shugar, D. H., Geertsema, M., Venditti, J. G., & Labay, K. (2018). Submarine Deposition of a Subaerial Landslide in Taan Fiord, Alaska. *Journal of Geophysical Research: Earth Surface*, *123*(10), 2443–2463. https://doi.org/10.1029/2018JF004608

Hall, K., & Thorn, C. E. (2014). Thermal fatigue and thermal shock in bedrock: An attempt to unravel the geomorphic processes and products. *Geomorphology*, *206*, 1–13. https://doi.org/10.1016/j.geomorph.2013.09.022

Hansen, L., L'heureux, J. S., & Longva, O. (2011). Turbiditic, clay-rich event beds in fjord-marine deposits caused by landslides in emerging clay deposits – palaeoenvironmental interpretation and role for submarine mass-wasting. *Sedimentology*, *58*(4), 890–915. https://doi.org/10.1111/j.1365-3091.2010.01188.x

Hastie, T., Tibshirani, R., & Friedman, J. (2009). *The Elements of Statistical Learning*. Springer. https://doi.org/10.1007/978-0-387-84858-7

He, K., Gkioxari, G., Dollár, P., & Girshick, R. (2017). Mask R-CNN. *2017 IEEE International Conference on Computer Vision (ICCV)*, 2980–2988. https://doi.org/10.1109/ICCV.2017.322

He, K., Zhang, X., Ren, S., & Sun, J. (2015, December 10). Deep Residual Learning for Image Recognition. https://doi.org/10.48550/arXiv.1512.03385

Higman, B., Lahusen, S. R., Belair, G. M., Staley, D. M., & Jacquemart, M. (2023). Inventory of Large Slope Instabilities, Prince William Sound, Alaska. https://doi.org/10.5066/P9XGMHHP

Higman, B., Shugar, D. H., Stark, C. P., Ekström, G., Koppes, M. N., Lynett, P., Dufresne, A., Haeussler, P. J., Geertsema, M., Gulick, S., Mattox, A., Venditti, J. G., Walton, M. A. L., McCall, N., Mckittrick, E., MacInnes, B., Bilderback, E. L., Tang, H., Willis, M. J., . . . Loso, M. (2018). The 2015 landslide and tsunami in Taan Fiord, Alaska. *Scientific Reports*, *8*(1), 12993. https://doi.org/10.1038/s41598-018-30475-w

Holm, K., Bovis, M., & Jakob, M. (2004). The landslide response of alpine basins to post-Little Ice Age glacial thinning and retreat in southwestern British Columbia. *Geomorphology*, *57*(3), 201–216. https://doi.org/10.1016/S0169-555X(03)00103-X

Huggel, C., Fischer, L., Schneider, D., & Haeberli, W. (2010). Research advances on climate-induced slope instability in glacier and permafrost high-mountain environments. *Geographica Helvetica*, *65*(2), 146–156. https://doi.org/10.5194/gh-65-146-2010

Huggel, C., Clague, J. J., & Korup, O. (2012). Is climate change responsible for changing landslide activity in high mountains? *Earth Surface Processes and Landforms*, *37*(1), 77–91. https://doi.org/10.1002/esp.2223

Hugonnet, R., McNabb, R., Berthier, E., Menounos, B., Nuth, C., Girod, L., Farinotti, D., Huss, M., Dussaillant, I., Brun, F., & Kääb, A. (2021). Accelerated global glacier mass loss in the early twenty-first century. *Nature*, *592*(7856), 726–731. https://doi.org/10.1038/s41586-021-03436-z

Hungr, O., Leroueil, S., & Picarelli, L. (2014). The Varnes classification of landslide types, an update. *Landslides*, *11*(2), 167–194. https://doi.org/10.1007/s10346-013-0436-y

Iverson, R. M. (2000). Landslide triggering by rain infiltration. *Water Resources Research*, *36*(7), 1897–1910. https://doi.org/10.1029/2000WR900090

Iverson, R. M., Reid, M. E., & LaHusen, R. G. (1997). Debris-flow mobilization from landslides. *Annual Review of Earth and Planetary Sciences*, *25*, 85–138. https://doi.org/10.1146/annurev.earth.25.1.85

Ivy-Ochs, S., Poschinger, A. V., Synal, H. A., & Maisch, M. (2009). Surface exposure dating of the Flims landslide, Graubünden, Switzerland. *Geomorphology*, *103*(1), 104–112. https://doi.org/10.1016/j.geomorph.2007.10.024

Kellndorfer, J., Cartus, O., Lavalle, M., Magnard, C., Milillo, P., Oveisgharan, S., Osmanoglu, B., Rosen, P. A., & Wegmüller, U. (2022a). Global seasonal Sentinel-1 interferometric coherence and backscatter data set. *Scientific Data*, *9*(1), 73. https://doi.org/10.1038/s41597-022-01189-6

Kellndorfer, J., Cartus, O., Lavalle, M., Magnard, C., Milillo, P., Oveisgharan, S., Osmanoglu, B., Rosen, P. A., & Wegmüller, U. (2022b). REST API: Global seasonal Sentinel-1 interferometric coherence and backscatter data set. https://gis.earthdata.nasa.gov/image/rest/services/GSSICB

Keyport, R. N., Oommen, T., Martha, T. R., Sajinkumar, K. S., & Gierke, J. S. (2018). A comparative analysis of pixel- and object-based detection of landslides from very high-resolution images. *International Journal of Applied Earth Observation and Geoinformation*, *64*, 1–11. https://doi.org/10.1016/j.jag.2017.08.015

Kos, A., Amann, F., Strozzi, T., Delaloye, R., von Ruette, J., & Springman, S. (2016). Contemporary glacier retreat triggers a rapid landslide response, Great Aletsch Glacier, Switzerland. *Geophysical Research Letters*, *43*(24), 12, 466–12, 474. https://doi.org/10.1002/2016GL071708

Krautblatter, M., Funk, D., & Günzel, F. K. (2013). Why permafrost rocks become unstable: a rock–ice-mechanical model in time and space. *Earth Surface Processes and Landforms*, *38*(8), 876–887. https://doi.org/10.1002/esp.3374

Lacroix, P., Belart, J. M. C., Berthier, E., Sæmundsson, Þ., & Jónsdóttir, K. (2022). Mechanisms of Landslide Destabilization Induced by Glacier-Retreat on Tungnakvíslarjökull Area, Iceland. *Geophysical Research Letters*, *49*(14). https://doi.org/10.1029/2022GL098302

Lawley, C. J. M., Giddy, P., Katz, L., Chu, N., Francis, A., Carvajal, J., Pinheiro, M., Tirona, K., Dettman, A., Chen, H., & Aucoin, F. (2024). Canada Geological Map Compilation. *Canada geological map compilation; Geological Survey of Canada, Open File 9169*. https://doi.org/https://doi.org/10.4095/pf995j5tgu

Le Roux, O., Schwartz, S., Gamond, J. F., Jongmans, D., Bourles, D., Braucher, R., Mahaney, W., Carcaillet, J., & Leanni, L. (2009). CRE dating on the head scarp of a major landslide (Séchilienne, French Alps), age constraints on Holocene kinematics. *Earth and Planetary Science Letters*, *280*(1), 236–245. https://doi.org/10.1016/j.epsl.2009.01.034

LeCun, Y., Bengio, Y., & Hinton, G. (2015). Deep learning. *Nature*, *521*(7553), 436–444. https://doi.org/10.1038/nature14539

Lei, Y., Gardner, A., & Agram, P. (2021). Autonomous Repeat Image Feature Tracking (autoRIFT) and Its Application for Tracking Ice Displacement. *Remote Sensing*, *13*(4), 749. https://doi.org/10.3390/rs13040749

Lemaire, E., Dufresne, A., Hamdi, P., Higman, B., Wolken, G. J., & Amann, F. (2024). Back-analysis of the paraglacial slope failure at Grewingk Glacier and Lake, Alaska. *Landslides*, *21*(4), 775–789. https://doi.org/10.1007/s10346-023-02177-6

Leroueil, S., & Locat, J. (1998). Slope movements — Geotechnical characterization, risk assessment and mitigation. In *Geotechnical Hazards* (p. 12). CRC Press.

Li, Z., Liu, F., Yang, W., Peng, S., & Zhou, J. (2022). A Survey of Convolutional Neural Networks: Analysis, Applications, and Prospects. *IEEE Transactions on Neural Networks and Learning Systems*, *33*(12), 6999–7019. https://doi.org/10.1109/TNNLS.2021.3084827

Liang, Y., Zhang, Y., Li, Y., & Xiong, J. (2023). Automatic Identification for the Boundaries of InSAR Anomalous Deformation Areas Based on Semantic Segmentation Model. *Remote Sensing*, *15*(21), 5262. https://doi.org/10.3390/rs15215262

Liu, T., Chen, T., Niu, R., & Plaza, A. (2021). Landslide Detection Mapping Employing CNN, ResNet, and DenseNet in the Three Gorges Reservoir, China. *IEEE Journal of Selected Topics in Applied Earth Observations and Remote Sensing*, *14*, 11417–11428. https://doi.org/10.1109/JSTARS.2021.3117975

Liu, Y., Yao, X., Gu, Z., Zhou, Z., Liu, X., Chen, X., & Wei, S. (2022). Study of the Automatic Recognition of Landslides by Using InSAR Images and the Improved Mask R-CNN Model in the Eastern Tibet Plateau. *Remote Sensing*, *14*(14), 3362. https://doi.org/10.3390/rs14143362

Løvholt, F., Pedersen, G., Harbitz, C. B., Glimsdal, S., & Kim, J. (2015). On the characteristics of landslide tsunamis. *Philosophical Transactions of the Royal Society A: Mathematical, Physical and Engineering Sciences*, *373*(2053), 20140376. https://doi.org/10.1098/rsta.2014.0376

Mahmud, Z. (2024). *Mask R-CNN for Object Detection and Instance Segmentation on Keras and TensorFlow 2.14.0 and Python 3.10.12*. Retrieved January 7, 2025, from https://github.com/z-mahmud22/Mask-RCNN_TF2.14.0

Marzeion, B., Cogley, J. G., Richter, K., & Parkes, D. (2014). Attribution of global glacier mass loss to anthropogenic and natural causes. *Science*, *345*(6199), 919–921. https://doi.org/10.1126/science.1254702

Matsuoka, N., & Murton, J. (2008). Frost weathering: recent advances and future directions. *Permafrost and Periglacial Processes*, *19*(2), 195–210. https://doi.org/10.1002/ppp.620

Maxar Technologies, Alaska Geospatial Office, & USGS. (2020). Alaska High Resolution Imagery (RGB). https://geoportal.alaska.gov/portal/home/item.html?id=d462231cc1454e1abb2dccd9a709a476

McColl, S., Davies, T., & McSaveney, M. (2010). Glacier retreat and rock-slope stability: debunking debuttressing. *Geologically Active*, 467–474.

McColl, S. T. (2012). Paraglacial rock-slope stability. *Geomorphology*, *153-154*, 1–16. https://doi.org/10.1016/j.geomorph.2012.02.015

McColl, S. T., & Davies, T. R. H. (2013). Large ice-contact slope movements: glacial buttressing, deformation and erosion. *Earth Surface Processes and Landforms*, *38*(10), 1102–1115. https://doi.org/10.1002/esp.3346

Michel, R., Avouac, J.-P., & Taboury, J. (1999). Measuring ground displacements from SAR amplitude images: Application to the Landers Earthquake. *Geophysical Research Letters*, *26*(7), 875–878. https://doi.org/10.1029/1999GL900138

Miller, D. J. (1960). The Alaska earthquake of July 10, 1958: Giant wave in Lituya Bay. *Bulletin of the Seismological Society of America*, *50*(2), 253–266. https://doi.org/10.1785/BSSA0500020253

Mitchell, T. M. (1997, March 1). *Machine Learning Tom Mitchell*. Retrieved January 28, 2025, from http://archive.org/details/machine-learning-tom-mitchell_202402

Mizukami, N., Newman, A. J., Littell, J. S., Giambelluca, T. W., Wood, A. W., Gutmann, E. D., Hamman, J. J., Gergel, D. R., Nijssen, B., Clark, M. P., & Arnold, J. R. (2022). New projections of 21st century climate and hydrology for Alaska and Hawaii. *Climate Services*, *27*, 100312. https://doi.org/10.1016/j.cliser.2022.100312

Molnar, P. (2004). Interactions among topographically induced elastic stress, static fatigue, and valley incision. *Journal of Geophysical Research: Earth Surface*, *109*. https://doi.org/10.1029/2003JF000097

Nava, L., Bhuyan, K., Meena, S. R., Monserrat, O., & Catani, F. (2022). Rapid Mapping of Landslides on SAR Data by Attention U-Net. *Remote Sensing*, *14*(6), 1449. https://doi.org/10.3390/rs14061449

Nava, L., Monserrat, O., & Catani, F. (2021). Improving Landslide Detection on SAR Data Through Deep Learning. *IEEE Geoscience and Remote Sensing Letters*, *19*, 1–5. https://doi.org/10.1109/LGRS.2021.3127073

Nichols, T. C., Jr. (1980). Rebound, its nature and effect on engineering works. *Quarterly Journal of Engineering Geology and Hydrogeology*, *13*(3), 133–152. https://doi.org/10.1144/GSL.QJEG.1980.013.03.01

Novellino, A., Pennington, C., Leeming, K., Taylor, S., Alvarez, I. G., McAllister, E., Arnhardt, C., & Winson, A. (2024). Mapping landslides from space: A review. *Landslides*, *21*(5), 1041–1052. https://doi.org/10.1007/s10346-024-02215-x

Oak, O., Nazre, R., Naigaonkar, S., Sawant, S., & Vaidya, H. (2024, August 3). A Comparative Analysis of CNN-based Deep Learning Models for Landslide Detection. https://doi.org/10.48550/arXiv.2408.01692

Obu, J., Westermann, S., Bartsch, A., Berdnikov, N., Christiansen, H. H., Dashtseren, A., Delaloye, R., Elberling, B., Etzelmüller, B., & Kholodov, A. (2019). Northern Hemisphere permafrost map based on TTOP modelling for 2000–2016 at 1 km2 scale. *Earth-Science Reviews*, *193*, 299–316. Retrieved January 28, 2025, from https://www.sciencedirect.com/science/article/pii/S0012825218305907

Obu, J., Westermann, S., Kääb, A., & Bartsch, A. (2018). Ground Temperature Map, 2000-2016, Northern Hemisphere Permafrost. https://doi.org/10.1594/PANGAEA.888600

Patton, A., Rathburn, S., Capps, D., Brown, R., & Singleton, J. (2020). Lithologic, geomorphic, and permafrost controls on recent landsliding in the Alaska Range. *Geosphere*, *16*(6), 1479–1494. https://doi.org/10.1130/GES02256.1

Pithan, F., & Mauritsen, T. (2014). Arctic amplification dominated by temperature feedbacks in contemporary climate models. *Nature Geoscience*, *7*(3), 181–184. https://doi.org/10.1038/ngeo2071

Plafker, G., & Berg, H. C. (1994, January 1). Overview of the geology and tectonic evolution of Alaska. In G. Plafker & H. C. Berg (Eds.), *The Geology of Alaska* (p. 0, Vol. G-1). Geological Society of America. https://doi.org/10.1130/DNAG-GNA-G1.989

Planet Labs. (2024). Planet Monthly Basemaps.

Porter, C., Howat, I., Noh, M.-J., Husby, E., Khuvis, S., Danish, E., Tomko, K., Gardiner, J., Negrete, A., Yadav, B., Klassen, J., Kelleher, C., Cloutier, M., Bakker, J., Enos, J., Arnold, G., Bauer, G., & Morin, P. (2023a). ArcticDEM - Mosaics, Version 4.1. https://doi.org/10.7910/DVN/3VDC4W

Porter, C., Howat, I., Noh, M.-J., Husby, E., Khuvis, S., Danish, E., Tomko, K., Gardiner, J., Negrete, A., Yadav, B., Klassen, J., Kelleher, C., Cloutier, M., Bakker, J., Enos, J., Arnold, G., Bauer, G., & Morin, P. (2023b). ArcticDEM Mosaic, Geoogle Arth Engine Data Catalog. Retrieved January 5, 2025, from https://developers.google.com/earth-engine/datasets/catalog/UMN_PGC_ArcticDEM_V3_2m_mosaic

Porter, C., Howat, I., Noh, M.-J., Husby, E., Khuvis, S., Danish, E., Tomko, K., Gardiner, J., Negrete, A., Yadav, B., Klassen, J., Kelleher, C., Cloutier, M., Bakker, J., Enos, J., Arnold, G., Bauer, G., & Morin, P. (2023c). Polar/ArcticDEM, REST API. Retrieved January 5, 2025, from https://elevation2.arcgis.com/arcgis/rest/services/Polar/ArcticDEM/ImageServer

Qin, H., Wang, J., Mao, X., Zhao, Z., Gao, X., & Lu, W. (2023). An Improved Faster R-CNN Method for Landslide Detection in Remote Sensing Images. *Journal of Geovisualization and Spatial Analysis*, *8*(1), 2. https://doi.org/10.1007/s41651-023-00163-z

Ravanel, L., & Deline, P. (2011). Climate influence on rockfalls in high-Alpine steep rockwalls: The north side of the Aiguilles de Chamonix (Mont Blanc massif) since the end of the 'Little Ice Age'. *The Holocene*, *21*(2), 357–365. https://doi.org/10.1177/0959683610374887

Reinthaler, J., & Paul, F. (2023). Using a Web Map Service to map Little Ice Age glacier extents at regional scales. *Annals of Glaciology*, 1–19. https://doi.org/10.1017/aog.2023.39

Ren, S., He, K., Girshick, R., & Sun, J. (2016, January 6). Faster R-CNN: Towards Real-Time Object Detection with Region Proposal Networks. https://doi.org/10.48550/arXiv.1506.01497

RGI Consortium. (2017). Randolph Glacier Inventory - A Dataset of Global Glacier Outlines, Version 6, 01 Alaska. https://doi.org/10.5067/F6JMOVY5NAVZ

RGI Consortium. (2023). Randolph Glacier Inventory - A Dataset of Global Glacier Outlines, Version 7, 01 Alaska. https://doi.org/10.5067/F6JMOVY5NAVZ

Sameen, M. I., & Pradhan, B. (2019). Landslide Detection Using Residual Networks and the Fusion of Spectral and Topographic Information. *IEEE Access*, *7*, 114363–114373. https://doi.org/10.1109/ACCESS.2019.2935761

Sanchez, G., Rolland, Y., Corsini, M., Braucher, R., Bourlès, D., Arnold, M., & Aumaître, G. (2010). Relationships between tectonics, slope instability and climate change: Cosmic ray exposure dating of active faults, landslides and glacial surfaces in the SW Alps. *Geomorphology*, *117*(1), 1–13. https://doi.org/10.1016/j.geomorph.2009.10.019

Scaioni, M., Longoni, L., Melillo, V., & Papini, M. (2014). Remote Sensing for Landslide Investigations: An Overview of Recent Achievements and Perspectives. *Remote Sensing*, *6*(10), 9600–9652. https://doi.org/10.3390/rs6109600

Schaefer, L. N., Coe, J. A., Wikstrom Jones, K., Collins, B. D., Staley, D. M., West, M., Karasozen, E., Miles, C., Wolken, G. J., Daanen, R. P., & Baxstrom, K. W. (2023). Kinematic Evolution of a Large Paraglacial Landslide in the Barry Arm Fjord of Alaska. *Journal of Geophysical Research: Earth Surface*, *128*(11). https://doi.org/10.1029/2023JF007119

Schaefer, L. N., Kim, J., Staley, D. M., Lu, Z., & Barnhart, K. R. (2024). *Satellite Interferometry Landslide Detection and Preliminary Tsunamigenic Plausibility Assessment in Prince William Sound, Southcentral Alaska* (No. 2023-1099) (ISSN: 2331-1258 Publication Title: Open-File Report). U.S. Geological Survey. https://doi.org/10.3133/ofr20231099

Schmidhuber, J. (2015). Deep learning in neural networks: An overview. *Neural Networks*, *61*, 85–117. https://doi.org/10.1016/j.neunet.2014.09.003

Shi, W., Zhang, M., Ke, H., Fang, X., Zhan, Z., & Chen, S. (2021). Landslide Recognition by Deep Convolutional Neural Network and Change Detection. *IEEE Transactions on Geoscience and Remote Sensing*, *59*(6), 4654–4672. https://doi.org/10.1109/TGRS.2020.3015826

Slaymaker, O. (2009). Proglacial, periglacial or paraglacial? *Geological Society, London, Special Publications*, *320*(1), 71–84. https://doi.org/10.1144/SP320.6

Slaymaker, O. (2011). Criteria to Distinguish Between Periglacial, Proglacial and Paraglacial Environments. *QUAGEO*, *30*(1), 85–94. https://doi.org/10.2478/v10117-011-0008-y

Storni, E., Hugentobler, M., Manconi, A., & Loew, S. (2020). Monitoring and analysis of active rockslide-glacier interactions (Moosfluh, Switzerland). *Geomorphology*, *371*, 107414. https://doi.org/10.1016/j.geomorph.2020.107414

Stumpf, A., Malet, J.-P., & Delacourt, C. (2017). Correlation of satellite image time-series for the detection and monitoring of slow-moving landslides. *Remote Sensing of Environment*, *189*, 40–55. https://doi.org/10.1016/j.rse.2016.11.007

Tehrani, F. S., Calvello, M., Liu, Z., Zhang, L., & Lacasse, S. (2022). Machine learning and landslide studies: recent advances and applications. *Natural Hazards*, *114*(2), 1197–1245. https://doi.org/10.1007/s11069-022-05423-7

Thorarinsson, S., Einarsson, T., & Kjartansson, G. (1959). On the Geology and Geomorphology of Iceland. *Geografiska Annaler*, *41*(2), 135–169. https://doi.org/10.1080/20014422.1959.11904385

Tofani, V., Segoni, S., Agostini, A., Catani, F., & Casagli, N. (2013). Technical Note: Use of remote sensing for landslide studies in Europe. *Natural Hazards and Earth System Sciences*, *13*(2), 299–309. https://doi.org/10.5194/nhess-13-299-2013

Trüssel, B. L., Motyka, R. J., Truffer, M., & Larsen, C. F. (2013). Rapid thinning of lake-calving Yakutat Glacier and the collapse of the Yakutat Icefield, southeast Alaska, USA. *Journal of Glaciology*, *59*(213), 149–161. https://doi.org/10.3189/2013J0G12J081

Ullo, S. L., Mohan, A., Sebastianelli, A., Ahamed, S. E., Kumar, B., Dwivedi, R., & Sinha, G. R. (2021). A New Mask R-CNN-Based Method for Improved Landslide Detection. *IEEE Journal of Selected Topics in Applied Earth Observations and Remote Sensing*, *14*, 3799–3810. https://doi.org/10.1109/JSTARS.2021.3064981

Varnes, D. J. (1978). Slope Mpvement Types and Processes. *Transportation Research Board Special Report*, (176). Retrieved January 2, 2025, from https://trid.trb.org/View/86168

Viles, H. A. (2013). Linking weathering and rock slope instability: non-linear perspectives. *Earth Surface Processes and Landforms*, *38*(1), 62–70. https://doi.org/10.1002/esp.3294

Wahr, J., Burgess, E., & Swenson, S. (2016). Using GRACE and climate model simulations to predict mass loss of Alaskan glaciers through 2100. *Journal of Glaciology*, *62*(234), 623–639. https://doi.org/10.1017/jog.2016.49

Walden, J., Jacquemart, M., Higman, B., Hugonnet, R., Manconi, A., & Farinotti, D. (2024). A regional analysis of paraglacial landslide activation in southern coastal Alaska [preprint]. *EGUsphere*, 1–38. https://doi.org/10.5194/egusphere-2024-1086

Walsh, J. E., & Brettschneider, B. (2019). Attribution of recent warming in Alaska. *Polar Science*, *21*, 101–109. https://doi.org/10.1016/j.polar.2018.09.002

Walsh, J. E., Redilla, K., Shippee, N., Cheung, L., Bigelow, D., & Wilcock, R. (2024). Projected Changes in Extreme Event Indices for Alaska [Number: 2 Publisher: Scientific Research Publishing]. *Atmospheric and Climate Sciences*, *14*(2), 191–209. https://doi.org/10.4236/acs.2024.142012

Wang, H., Zhang, L., Yin, K., Luo, H., & Li, J. (2021). Landslide identification using machine learning. *Geoscience Frontiers*, *12*(1), 351–364. https://doi.org/10.1016/j.gsf.2020.02.012

White, J. H., Walsh, J. E., & Thoman Jr, R. L. (2021). Using Bayesian statistics to detect trends in Alaskan precipitation. *International Journal of Climatology*, *41*(3), 2045–2059. https://doi.org/10.1002/joc.6946

Wiles, G. C., & Calkin, P. E. (1992). Reconstruction of a debris-slide-initiated flood in the southern Kenai Mountains, Alaska. *Geomorphology*, *5*(6), 535–546. https://doi.org/10.1016/0169-555X(92)90024-I

Wilson, F. H., Hults, C. P., Mull, C. G., & Karl, S. M. (2015). Geologic map of Alaska. *Geologic map of Alaska: U.S. Geological Survey Scientific Investigations Map 3340, 197 p., 2 sheets, scale 1:584,000*. https://doi.org/,197p.,2sheets,scale1:584,000,http://dx.doi.org/10.3133/sim3340.

Zeiler, M. D., & Fergus, R. (2013). Visualizing and Understanding Convolutional Networks. https://doi.org/10.48550/arXiv.1311.2901

Zhang, Y., Chu, J., Leng, L., & Miao, J. (2020). Mask-Refined R-CNN: A Network for Refining Object Details in Instance Segmentation. *Sensors*, *20*(4), 1010. https://doi.org/10.3390/s20041010

Zhao, C., & Lu, Z. (2018). Remote Sensing of Landslides—A Review. *Remote Sensing*, *10*(2), 279. https://doi.org/10.3390/rs10020279

Zhao, X., Wang, L., Zhang, Y., Han, X., Deveci, M., & Parmar, M. (2024). A review of convolutional neural networks in computer vision. *Artificial Intelligence Review*, *57*(4), 99. https://doi.org/10.1007/s10462-024-10721-6

Zhong, C., Liu, Y., Gao, P., Chen, W., Li, H., Hou, Y., Nuremanguli, T., & Ma, H. (2020). Landslide mapping with remote sensing: challenges and opportunities. *International Journal of Remote Sensing*, *41*(4), 1555–1581. https://doi.org/10.1080/01431161.2019.1672904

A. Model evaluation metrics per epoch

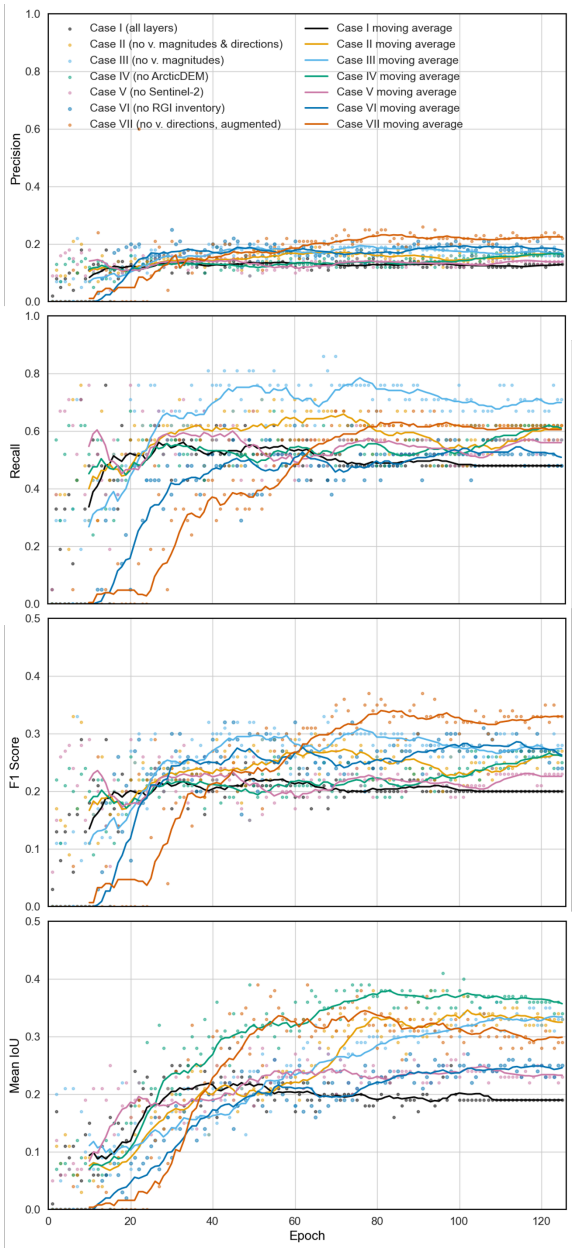

Figure A.0.1: Evolution of model evaluation metrics across the different epochs for the different input data cases in assessment on the validation data.

Personal declaration

I hereby declare that the submitted thesis is the result of my own, independent work. All external sources are explicitly acknowledged in the thesis.

Speicher, 31.01.2025

Jérôme Messmer